adata, citation and similar papers at core.ac.uk

brought to you by

provided by Archivio della ricerca- Università di Roma

World Scientific
www.worldscientific.com

JAPAN SOCIETY OF CIVIL ENGINEERS
COASTAL ENGINEERING COMMITTEE

Coastal Engineering Journal, Vol. 58, No. 3 (2016) 1650011 (50 pages)
© The Author(s)
DOI: 10.1142/S057856341650011X

Coast. Eng. J. 2016.58. Downloaded from www.worldscientific.com
by UNIVERSITA DEGLI STUDI DI ROMA on 10/19/16. For personal use only.

Modeling Bed Evolution Using Weakly Coupled Phase-Resolving Wave Model and Wave-Averaged Sediment Transport Model

Francesco Gallerano*, Giovanni Cannata, Oriana De Gaudenzi and Simone Scarpone

Department of Civil, Constructional and Environmental Engineering,
University of Rome 'La Sapienza',
Via Eudossiana 18, 00184 Roma, Italy
**francesco.gallerano@uniroma1.it*

Received 5 November 2015
Accepted 28 July 2016
Published 29 September 2016

In this paper, we propose a model for the simulation of the bed evolution dynamics in coastal regions characterized by articulated morphologies. An integral form of the fully nonlinear Boussinesq equations in contravariant formulation, in which Christoffel symbols are absent, is proposed in order to simulate hydrodynamic fields from deep water up to just seaward of the surf zones. Breaking wave propagation in the surf zone is simulated by integrating the nonlinear shallow water equations with a high-order shock-capturing scheme. The near-bed instantaneous flow velocity and the intra-wave hydrodynamic quantities are calculated by the momentum equation integrated over the turbulent boundary layer. The bed evolution dynamics is calculated starting from the contravariant formulation of the advection–diffusion equation for the suspended sediment concentration in which the advective sediment transport terms are formulated according to a quasi-three-dimensional approach, and taking into account the contribution given by the spatial variation of the bed load transport. The model is validated against several tests by comparing numerical results with experimental data. The ability of the proposed model to represent the sediment transport phenomena in a morphologically articulated coastal region is verified by

*Corresponding author.

This is an Open Access article published by World Scientific Publishing Company. It is distributed under the terms of the Creative Commons Attribution 4.0 (CC-BY) License. Further distribution of this work is permitted, provided the original work is properly cited.

numerically simulating the long-term bed evolution in the coastal region opposite Pescara harbor (in Italy) and comparing numerical results with the field data.

Keywords: Phase-resolving model; undertow; intra-wave quantities; sediment transport; bed evolution dynamics.

Coast. Eng. J. 2016.58. Downloaded from www.worldscientific.com
by UNIVERSITA DEGLI STUDI DI ROMA on 10/19/16. For personal use only.

List of Symbols

H : total local water depth
h : local still water depth
η : local surface displacement
σ : arbitrary distance from the still water surface
$\vec{u}$: horizontal velocity
$\vec{u}_\alpha$: horizontal velocity at an arbitrary distance from the still water level
$\vec{u}_2$: second order term in depth power expansion of $\vec{u}$
∇ : two-dimensional differential operator
$\vec{r}$: conservative variable
$\vec{s}$: conservative variable
$\vec{V}'$: dispersive term
$\vec{x}$: Cartesian coordinates
x^l : contravariant components of the Cartesian coordinates
$\vec{\xi}$: curvilinear coordinates
ξ^l : contravariant components of the curvilinear coordinates
$\vec{g}^{(l)}$: contravariant base vectors
$\vec{g}_{(l)}$: covariant base vectors
g_{lm} : metric tensor
g^{lm} : inverse of the metric tensor
$\sqrt{g}$: Jacobian of the coordinates transformation
$\vec{b}$: generic vector in the Cartesian coordinate system
b^l : contravariant components of $\vec{b}$
b_l : covariant components of $\vec{b}$
$b^l_{,m}$: covariant derivative of b^l
Γ^l_{mk} : christoffel symbol
r^{*l} : contravariant components of $\vec{r}^*$
$\vec{\tilde{g}}^{(l)}$: contravariant base vector defined at a given point
λ_k : covariant components of $\vec{\tilde{g}}^{(l)}$
G : constant of gravity
V'^k, V''^k, T^k : contravariant components of the dispersive terms
W^k : contravariant components of the second order term of the vertical component of the vorticity
R^k : contravariant components of the bottom resistance term
u^l : contravariant components of the horizontal velocity

u_α^l : contravariant components of $\vec{u}_\alpha$
u_B^l : contravariant component of the corrective velocity
δ : wave boundary layer thickness
u_f : friction velocity
z : generic height inside the wave boundary layer
U : horizontal velocity magnitude
U_δ : horizontal velocity magnitude calculated at the top of the wave boundary layer
k : bed roughness
d_{50} : sediment mean diameter
K : von Karman constant
T : wave period
τ : bed shear stress
$\widetilde{u_{fc}}$: current friction velocity
k_t : turbulent kinetic energy
σ_k : Prandt number
c_d : coefficient for the dissipation term
l : length scale of turbulence
$\nu_{t,f}$: wave breaking eddy viscosity
ν_t : total eddy viscosity
K_d : diffusion coefficient
C : suspended sediment concentration
D : sediment deposition rate
P : sediment pick-up rate
w_{sed} : sediment fall velocity
$\tilde{C}_a$: actual concentration
C_R : reference concentration
a : reference height
$q_{bc,\text{net}}$: net cross-shore sediment transport rate from the swash zone
K_c : empirical coefficient
Φ_m : friction angle for a moving grain
β_e : foreshore equilibrium slope
u_0 : propagation velocity of the wet and dry front
z_f : bed elevation
p : sediment porosity

Coast. Eng. J. 2016.58. Downloaded from www.worldscientific.com
by UNIVERSITA DEGLI STUDI DI ROMA on 10/19/16. For personal use only.

1. Introduction

In the design of coastal structures, long-term bed evolution predictions play a key role. The simulation of the bed evolution dynamics implies an appropriate representation of sediment particle resuspension and settling phenomena which are

mainly related to wave refraction, shoaling, diffraction, reflection, wave breaking phenomena, to long-shore and rip currents, to the hydrodynamic field three-dimensionality, hydrodynamic quantities variability and run-up and run-down phenomena in the swash zone.

Coastal currents and, more generally, hydrodynamic phenomena produced by wave motion have features of three-dimensionality that are locally important [Choi and Yoon, 2008; Li *et al.*, 2007; Ma *et al.*, 2014; Wai *et al.*, 2004]. The sediment transport in coastal regions is consequently the result of the above-mentioned three-dimensional hydrodynamic processes, driven by hydrodynamic quantities that are time-varying into the wave period and is influenced by the net sediment transport rate from the swash zone in the cross-shore direction.

The most important of the above three-dimensional phenomena and the cause of offshore sediment transport is the undertow, which consists of a circulation in the vertical plane in which the near-bed current velocities are offshore-directed in the surf zone [Deigaard *et al.*, 1991; Nam *et al.*, 2014; Rakha, 2002]. In particular, the wave-averaged horizontal velocities are characterized by uniform distribution below the mean trough level and by a direction opposite to that of the horizontal velocity above the mean trough level. Such near-bed current velocities are the cause of the cross-shore sediment transport and bar formation.

In combined wave–current motion and outside the surf zone, sediment transport phenomena are conditioned by a complex turbulence structure and by the flow velocities in proximity of the bottom, where the sediment is usually picked up by the waves and transported by the current. Inside the surf zone, the sediment particle resuspension and transport are conditioned, as well as by a complex turbulence structure and the near-bed flow velocities, also by the surface generated turbulence due to the wave breaking.

In particular in combined wave–current motion, the unsteady flow is characterized by a boundary layer which develops every time the flow reverses: the sediment particle resuspension process develops during the large near-bed velocities; the sediment is carried away from the bed at the end of each half of the wave cycle; when the flow reverses the sediment settles and it is entrained into the boundary layer. Consequently, it is not difficult to emphasize that the simulation of the sediment particle resuspension, settling and transport phenomena needs to take into account the variability in the wave period of the intra-wave hydrodynamic quantities, such as: the wave boundary layer thickness, friction velocity, bed shear stress, turbulence inside the wave boundary layer and the turbulence outside the wave boundary layer produced by currents and wave breaking [Fredsøe, 1984; Fredsøe *et al.*, 1985; Deigaard *et al.*, 1986; Shibayama and Nistor, 1998].

Furthermore, as mentioned, morphodynamic changes are influenced by the contribution to transported material from the swash zone which, in turn, depends on the representative hydrodynamic quantities of the swash zone, in particular on the maximum uprush, flow velocity and duration of swash events.

Coast. Eng. J. 2016.58. Downloaded from www.worldscientific.com
by UNIVERSITA DEGLI STUDI DI ROMA on 10/19/16. For personal use only.

From the previous synthetic considerations the fact emerges that, if one want to represent the bed evolution dynamics for a long time scale in the vicinity of the morphologically articulated coastline and in the presence of coastal structures, it is necessary to take into account three fundamental aspects. The first aspect concerns the simulation of the sediment transport phenomena produced by undertow; the second aspect concerns the simulation of sediment particle resuspension and settling phenomena associated with intra-wave hydrodynamic quantities and the complex turbulence structure under a nonbreaking and breaking wave; the third aspect concerns the calculation of the net cross-shore sediment transport rate from the swash zone.

In literature, the simulation of bed morphological change phenomena is placed within the context defined by one-way coupling two-phase flow dynamic representations, where a fluid phase drives a solid phase assumed as a continuum: consequently the simulation of these phenomena, in literature, is generally performed by a first model for the simulation of the hydrodynamic quantities and a second model for the simulation of the sediment particle resuspension, settling and transport and of the bed morphological change. Within the time scale of a several storm events, rip channels can evolve and sand banks can migrate. These bathymetric changes are caused by waves and currents, which, in turn, are affected by changes in the bathymetry. Hence, studying the bed evolution requires an alternate coupling, at a high rate of exchange of up-to-date data, between hydrodynamic models (waves and currents) and morphodynamic models (sediment transport and bathymetry updates).

In the design of coastal structures, the long-term bed evolution prediction runs into a contradiction. On the one hand, there is the need to simulate the variability, during the wave period and three-dimensionally, of the intra-wave hydrodynamic quantities (which intervene in the characterization of the complex turbulent phenomena occurring in combined wave–current motion, and that, in turn, affect the sediment particle resuspension, settling and transport processes); on the other hand, there is the need to perform long-term simulations by an alternating coupling at a high rate of exchange of up-to-date data between hydrodynamic models (waves and currents) and morphodynamic models (sediment transport and bathymetry updates).

As mentioned, coastal currents and, more generally, hydrodynamic phenomena produced by wave motion have features of three-dimensionality that are locally important. However, the long-term bed evolution simulations, in literature are performed representing the current circulations in terms of two-dimensional flows in the horizontal plane obtained by a depth-average operation of the three-dimensional motion equations. Such two-dimensional models for the long-term simulations actually represent a reasonable level of compromise, in terms of computational effort and achievable result accuracy, between the more traditional techniques and the most advanced three-dimensional models [Ma *et al.*, 2014].

Pioneers in the study of coastal circulations produced by the wave breaking are Longuet-Higins and Stewart [1964], whose works led to the development of

Coast. Eng. J. 2016.58. Downloaded from www.worldscientific.com
by UNIVERSITA DEGLI STUDI DI ROMA on 10/19/16. For personal use only.

two-dimensional models in which the motion equations are depth-averaged and wave-averaged. These models, which are defined hereafter as two-dimensional wave-averaged (2DWA), do not explicitly represent the oscillatory characteristics of the wave motion but its own average effect on the wave-averaged kinematic quantities. The 2DWA models are based on the use of radiation stresses.

The 2DWA models are not able to directly simulate the undertow, which is produced by those hydrodynamic phenomena related to wave shape modification in the surf zone.

The 2DWA models require a wave theory to describe the intra-wave hydrodynamic quantities varying on the wave period. In case of random waves, the 2DWA models need to introduce *ad hoc* parameterization, in order to take into account the wave shape changes (nonbreaking or breaking wave) in the computing of intra-wave hydrodynamic variables.

The 2DWA models are not able to directly represent the hydrodynamics of the swash zone: consequently such models must adopt simplified representations of the run-up and run-down phenomena [Mather *et al.*, 2011].

In order to simulate the bed evolution dynamics, many authors such as Dronen and Deigaard [2007], Nam *et al.* [2009, 2011] simulated the wave-produced hydrodynamic fields by using the 2DWA model and calculated the intra-wave hydrodynamic variables starting from the depth-averaged velocity and wave orbital velocity at the bottom evaluated by the potential theory. Furthermore, in order to predict the swash zone transport rate Nam *et al.* [2009] derived the hydrodynamics in the swash zone from the ballistic theory proposed by Larson and Wamsley [2007].

A further development in the two-dimensional hydrodynamic models is represented by two-dimensional phase-resolving (2DPR) models that explicitly represent the periodicity of the wave motion and are based on the integration of Boussinesq equations which arise from the depth integration of the Euler equations once the depth dependence of the variables is known. One of the advantages of these models is that there is no need to decouple the wave and current motion and thus no need to compute the radiation stresses for a separate run of the wave-averaged model.

Many authors [Kennedy *et al.*, 2000; Hsiao and Hsu, 2011; Mohsin and Tajima, 2014] introduced into the Boussinesq equations breaking dissipation terms which need to be parameterized and have to be applied in the surf zone. As the weak solutions of the integral form of the nonlinear shallow water equations (NSWE) (numerically solved by a shock-capturing scheme) are able to directly represent wave breaking, the explicit introduction in the equations of terms representing the breaking wave dissipation is not necessary. Shock-capturing schemes permit an explicit simulation of the wave breaking phenomenon, thus these schemes do not require any empirical calibration [Shi *et al.*, 2012]. Furthermore the above-mentioned shock-capturing schemes for the solution of NSWE are able to effectively calculate the hydrodynamic quantities in the swash zone.

Coast. Eng. J. 2016.58. Downloaded from www.worldscientific.com
by UNIVERSITA DEGLI STUDI DI ROMA on 10/19/16. For personal use only.

The 2DPR models make it possible to take into account the coastal breaking wave-induced circulations, the nonlinear wave–wave interactions and the fully coupled wave–current interactions. In general, these models are able to capture some three-dimensional aspects like the undertow and the variability in the wave period of the hydrodynamic quantities, and to calculate the hydrodynamic quantities in the swash zone; such models therefore make it possible to simulate the main hydrodynamic phenomena that affect the sediment particle resuspension, settling and transport.

In the surf zone, the wave-average of the instantaneous horizontal velocity vertical profiles (which are predicted by most of the Boussinesq models involving breaking dissipation terms in the momentum equation and NSWE solved by shock-capturing schemes) gives horizontal velocities which are characterized by uniform distribution below the mean trough level and by a direction opposite to that of the horizontal velocity above the mean trough level. Hence, the above-mentioned models are able to capture the undertow.

Furthermore, the intra-wave hydrodynamic processes are included in the 2DPR models and need not be parameterized, as is required in the 2DWA models. The 2DPR models are therefore able to represent the variability in the wave period of the hydrodynamic quantities that directly intervene in the sediment particle resuspension and settling.

The 2DPR models can directly simulate the run-up and run-down hydrodynamic phenomena in the swash zone in order to represent the cross-shore sediment transport phenomena in the aforementioned zone.

Some models for the simulation of the bed evolution dynamics are based on the Exner sediment continuity equation [Kalinske, 1947], in which the time variation of the bottom is related to the variation in the cross-shore and long-shore direction of the suspended sediment load.

The models which use the Exner sediment continuity equation are based on the assumption that the suspended sediment load is a function of the local conditions; consequently the resulting equilibrium transport rates are described by empirical or semi-empirical expressions which are introduced in the above equation. Such models evolve from the hypothesis that sediment particle has time to reach a state of equilibrium with the local conditions.

Other models solve the wave-averaged advection–diffusion equation for the depth-averaged suspended sediment concentration (these models are indicated hereafter with the contraction 2DHC) to yield the dynamic sediment load. Such schemes are more appropriate for finer sediment because the suspended sediment is distributed throughout a larger proportion of the water column and hence does not have time to reach a state of equilibrium in spatially-varying flow conditions. These models take into account the pick-up rate, sediment deposition rate, sediment convection and diffusion. Nam *et al.* [2009] indicated that the wave-averaged advection–diffusion equation for the depth-averaged suspended sediment concentration can be

Coast. Eng. J. 2016.58. Downloaded from www.worldscientific.com
by UNIVERSITA DEGLI STUDI DI ROMA on 10/19/16. For personal use only.

applied to situations where concentration changes in time and space at a high rate, for example, at river mouths, tidal inlets, and in the vicinity of structures. Moreover, Hsu *et al.* [2006] emphasized that the use of the above equation is made necessary in order to also represent those situations characterized by a phase lag between flow forcing and bottom stress and between stress and transport.

Nam *et al.* [2009, 2011] used a 2DWA hydrodynamic model and a 2DHC sediment transport model: they solved the wave-averaged advection–diffusion equation for the depth-averaged suspended sediment concentration in which the sediment pick-up is related to the bottom reference concentration calculated using the potential theory, and the deposition rate is related to the depth-averaged concentration and to the vertically uniform eddy viscosity coefficient following the line shown by Camenen and Larson [2008]. They also used the sediment transport rate at the still water shoreline obtained from the swash zone computations as boundary condition for computing the suspended sediment load in the surf zone.

In the 2DHC models, the advective sediment transport terms are expressed as a function of the product of the depth and wave-averaged horizontal velocity and the depth and wave-averaged suspended sediment concentration (2DHC approach). Consequently, these models are not able to directly reap the three-dimensional sediment transport features and in particular the cross-shore suspended sediment transport due mainly to the undertow. Again in these models, if the hydrodynamic model is a 2DWA type and the sediment pick-up rate term is related to the reference concentration, this latter is calculated using the intra-wave hydrodynamic variables obtained by the potential theory. Thus, calculating the sediment pick-up rate term is a representative of regular wave conditions. In addition in these models, the contribution to transported material from the swash zone must be considered using empirical formulas, not having direct simulations of hydrodynamic phenomena in the swash zone.

In reality, both the horizontal velocity and concentration vertical profiles are not uniform. The depth-integrated product of the horizontal velocity vertical profile and concentration vertical profile (Q3D approach) is the basis of the quasi-three-dimensional models for the simulation of the bed evolution dynamics; these models are able to take into account the cross-shore suspended sediment transport related to the undertow, time variability of the intra-wave hydrodynamic quantities and cross-shore suspended sediment transport from the swash zone.

Dronen and Deigaard [2007] used a 2DWA hydrodynamic model and a morphological model which solves the Exner equation. The Q3D approach intervenes in the formalization of the above equation since the wave-averaged suspended sediment load is given by the time-averaged depth integral of the product of the instantaneous horizontal velocity and instantaneous concentration. Rakha [1998] used a 2DPR hydrodynamic model and solved the Exner equation with a Q3D approach. In the Exner equation, the wave-averaged suspended sediment load is given by the time-averaged depth integral of the product of the instantaneous horizontal velocity

Coast. Eng. J. 2016.58. Downloaded from www.worldscientific.com
by UNIVERSITA DEGLI STUDI DI ROMA on 10/19/16. For personal use only.

and instantaneous concentration. In calculating such suspended sediment load, the wave velocity due to oscillatory motion and the vertical variation of mean undertow are included.

In this work, a model for the simulation of bed evolution dynamics is presented and consists of two parts: a first 2DPR model that makes it possible to consider some three-dimensional aspects of the hydrodynamic fields such as the undertow, to calculate the intra-wave hydrodynamic variables and to simulate the run-up and run-down phenomena in the swash zone, and a second morphodynamic model based on the wave-averaged advection–diffusion equation for the suspended sediment concentration with a Q3D approach.

An integral contravariant formulation for the governing equations is proposed in order to permit the numerical integration of the above-mentioned equations on generalized curvilinear grids representing the articulated morphology of real coastal regions.

The phase-resolving hydrodynamic model solves the fully nonlinear Boussinesq equations (FNBEs) from deep water up to just seaward of the surf zones and the NSWE in the surf zones.

The simulation of coastal hydrodynamic phenomena on computational domains representing the complexity of real morphologies can be made either by using unstructured grids [Mandal and Rao, 2011; Cioffi and Gallerano, 2012; Titarev and Drikakis, 2011] or by using computational grids obtained from the intersection of boundary conforming coordinate lines. By using curvilinear grids, the motion equations can be written in contravariant formulation [Luo and Bewley, 2004; Gallerano and Cannata, 2011b]. Curvilinear models based on the solution of the shallow water equations were presented by Shi and Sun [1995] and Shi *et al.* [1998].

In this paper, a new integral form of the FNBEs in contravariant formulation, in which Christoffel symbols are absent, is proposed in order to simulate hydrodynamic fields from deep water up to just seaward of the surf zones. The above-mentioned motion equations retain the term related to the second-order vertical vorticity. Breaking wave propagation in the surf zone is simulated by integrating the NSWE with a high-order shock-capturing scheme: an exact Riemann solver and a weighted essentially nonoscillatory (WENO) reconstruction technique are used.

In order to take into account the sediment transport in the swash zone, a new procedure for the simulation of the uprush and backwash dynamics of the wet and dry front is proposed.

From the horizontal velocity vertical profile obtained by the proposed hydrodynamic model and from the integration of the momentum equation over the wave boundary layer, the near-bed velocity, the instantaneous boundary layer thickness, the friction velocity and the bed shear stress are calculated. The calculation of the eddy viscosity vertical distribution is carried out by following the conceptual line proposed by Fredsøe *et al.* [1985] and Deigaard *et al.* [1986] and used by Rakha

Coast. Eng. J. 2016.58. Downloaded from www.worldscientific.com
by UNIVERSITA DEGLI STUDI DI ROMA on 10/19/16. For personal use only.

[1998]. In particular, under breaking waves, the instantaneous eddy viscosity vertical distribution is calculated by taking into account the turbulence contribution due to the wave boundary layer, current and wave breaking.

Bed evolution dynamics is calculated starting from the contravariant formulation of the advection–diffusion equation for the suspended sediment concentration. The advective sediment transport terms that appear in the above equation are formulated according to a Q3D approach and are calculated starting from the depth-integrated product of the horizontal velocity and concentration the vertical distributions, in order to take into account the sediment transport related to the undertow. The sediment pick-up rate source term is expressed as a function of the instantaneous reference concentration calculated by the Zyserman and Fredsøe [1994] formula related to the intra-wave hydrodynamic variables. The time bottom variation is related to the contribution given by the product of the settling velocity and the difference between reference concentration and actual concentration (at a distance a from the bottom) and to the contribution given by the spatial variation of the bed load transport.

The sediment transport in the swash zone is evaluated through the procedure proposed by Larson and Wamsley [2007], which involves the hydrodynamic quantities produced by the wet and dry front dynamics simulation in the swash zone.

The computing of the long-term bed evolution is carried out by a sequence that alternates, at each step (morphological step), the simulation of wave and current velocity fields and the simulation of the sediment transport and bed morphological change. The values of the hydrodynamic quantities, calculated by the hydrodynamic phase-resolving model, are used as input data in the sediment transport and morphological change model; the bathymetry thus modified intervenes as input condition for the calculation of waves and currents by the phase-resolving model in the next morphological step.

2. Description of the Model for the Simulation of the Bed Evolution Dynamics

The model for the simulation of the bed evolution dynamics here presented is part of the one-way coupling two-phase flow dynamics representations. The model consists of two parts: a first 2DPR model that makes it possible to calculate the intra-wave hydrodynamic variables, to consider some of the three-dimensional aspects of the hydrodynamic fields and to simulate the run-up and run-down phenomena in the swash zone; a second model for the sediment transport and bed morphological change simulation in which the advection–diffusion equation for the suspended sediment concentration with a Q3D approach is resolved.

The governing equations are written in an integral contravariant formulation in order to permit the numerical solution of the above-mentioned equations on generalized curvilinear grids representing the articulated morphology of real coastal regions.

Coast. Eng. J. 2016.58. Downloaded from www.worldscientific.com
by UNIVERSITA DEGLI STUDI DI ROMA on 10/19/16. For personal use only.

Coast. Eng. J. 2016.58. Downloaded from www.worldscientific.com
by UNIVERSITA DEGLI STUDI DI ROMA on 10/19/16. For personal use only.

2.1. *Hydrodynamic model*

The hydrodynamic model is based on the scheme proposed by Gallerano *et al.* [2014] for the solution of the FNBEs in contravariant form.

Let $H = h + \eta$ be the total local water depth, where h is the local still water depth and η is the local surface displacement. Using a Taylor expansion of the velocity about an arbitrary distance from the still water surface, σ, and assuming zero horizontal vorticity, as proposed by Nwogu [1993], Wei *et al.* [1995], the vertical distribution of the horizontal velocity can be written as

$$\vec{u}(z) = \vec{u}_\alpha + \vec{u}_2(z), \tag{1}$$

where $\vec{u}_\alpha$ is the horizontal velocity at an arbitrary distance from the still water level and $\vec{u}_2(z) = (\sigma - z)\nabla[\nabla \cdot (h\vec{u}_\alpha)] + [(\sigma^2/2) - (z^2/2)]\nabla(\nabla \cdot \vec{u}_\alpha)$ consists of the second order terms in depth power expansion of the velocity vector in which ∇ is the two-dimensional differential operator defined as $\nabla = (\partial/\partial x, \partial/\partial y)$ in a Cartesian reference system.

The following vectors can be defined: $\vec{r} = H\vec{u}_\alpha$ and $\vec{s} = H\vec{u}_2$, in which $\vec{u}_2$ is the depth-averaged value of $\vec{u}_2(z)$. The auxiliary variable $\vec{r}^*$ is introduced and defined as

$$\vec{r}^* = \vec{r} + H\vec{V}' \tag{2}$$

The explicit expressions of $\vec{s}$ and of $\vec{V}'$ are shown in Appendix A.

We consider a transformation $x^l = x^l(\xi^1, \xi^2)$ from the Cartesian coordinates $\vec{x}$ to the curvilinear coordinates $\vec{\xi}$ (note that hereinafter the superscript indicates the generic component and not the powers). Let $\vec{g}_{(l)} = \partial\vec{x}/\partial\xi^l$ be the covariant base vectors and $\vec{g}^{(l)} = \partial\xi^l/\partial\vec{x}$ the contravariant base vectors. The metric tensor and its inverse are defined, respectively, by $g_{lm} = \vec{g}_{(l)} \cdot \vec{g}_{(m)}$ and $g^{lm} = \vec{g}^{(l)} \cdot \vec{g}^{(m)}$ $(l, m = 1, 2)$. The Jacobian of the transformation is $\sqrt{g} = \sqrt{\det(g_{lm})}$. The transformation relationships between the components of the generic vector $\vec{b}$ in the Cartesian coordinate system and its contravariant and covariant components, b^l and b_l, in the curvilinear coordinate system are given by

$$b^l = \vec{g}^{(l)} \cdot \vec{b}, \quad \vec{b} = b^l\vec{g}_{(l)}; \quad b_l = \vec{g}_{(l)} \cdot \vec{b}, \quad \vec{b} = b_l\vec{g}^{(l)}. \tag{3}$$

In the following equations, a comma with an index in a subscript stands for covariant differentiation.

Let r^{*l} be the lth contravariant component of the vector $\vec{r}^*$

$$r^{*l} = r^l + HV'^l. \tag{4}$$

Let ΔA be the area of the generic surface element and $\vec{\tilde{g}}^{(l)} = \vec{g}^{(l)}(\xi_0^1, \xi_0^2)$ the contravariant base vector defined at point $P_0 \in \Delta A$ whose coordinates are ξ_0^1 and ξ_0^2.

The integral contravariant form of the FNBEs can be expressed as

$$\iint_{\Delta A} \frac{\partial H}{\partial t} dA + \int_L r^m n_m dL = -\iint_{\Delta A} (s^l)_{,l} dA, \tag{5}$$

$$\iint_{\Delta A} \vec{\tilde{g}}^{(l)} \cdot \vec{g}_{(k)} \frac{\partial r^{*k}}{\partial t} dA + \int_L \left(\vec{\tilde{g}}^{(l)} \cdot \vec{g}_{(k)} \frac{r^k r^m}{H} + G \vec{\tilde{g}}^{(l)} \cdot \vec{g}^{(m)} \frac{H^2}{2} \right) n_m dL$$
$$= \iint_{\Delta A} \vec{\tilde{g}}^{(l)} \cdot \vec{g}_{(k)} G H g^{km} h_{,m} dA - \iint_{\Delta A} \vec{\tilde{g}}^{(l)} \cdot \vec{g}_{(k)} R^k dA$$
$$- \iint_{\Delta A} \vec{\tilde{g}}^{(l)} \cdot \vec{g}_{(k)} \frac{r^k}{H} (s^m)_{,m} dA + \iint_{\Delta A} \vec{\tilde{g}}^{(l)} \cdot \vec{g}_{(k)} \frac{\partial H}{\partial t} V'^k dA$$
$$- \iint_{\Delta A} \vec{\tilde{g}}^{(l)} \cdot \vec{g}_{(k)} H V''^k dA - \iint_{\Delta A} \vec{\tilde{g}}^{(l)} \cdot \vec{g}_{(k)} H T^k dA$$
$$- \iint_{\Delta A} \vec{\tilde{g}}^{(l)} \cdot \vec{g}_{(k)} H W^k dA, \tag{6}$$

where G is the constant of gravity, L is the contour line of ΔA and n_m is the mth component of the covariant outward normal. V'^k, V''^k and T^k are the kth contravariant component of the dispersive terms obtained by retaining terms up to $O(\mu^2)$ and $O(\varepsilon\mu^2)$ in depth power expansions of the horizontal velocity according to Wei *et al.* [1995], W^k is the kth contravariant component of the term related to the approximation to the second-order of the vertical component of the vorticity and R^k is the kth contravariant component of the bottom resistance term. In Eq. (5), the second term on the left-hand side is the flux term. In Eq. (6), the second term on the left-hand side is the flux term, the first term on the right-hand side is the source term related to the bottom slope, the second term on the right-hand side R^k, as mentioned, is the bottom resistance term approximated by a quadratic law.

Expressions for terms s^l, V'^l, V''^l, T^l and W^l are given in Appendix A.

Equations (5) and (6) represent the integral expressions of the FNBEs in contravariant formulation in which Christoffel symbols are absent. The procedure for the formulation of the above-mentioned contravariant integral equations is clarified in Gallerano and Cannata [2011a]. These equations are accurate to $O(\mu^2)$ and $O(\varepsilon\mu^2)$ in dispersive terms and retain the conservation of potential vorticity up to $O(\mu^2)$, in accordance with the formulation proposed by Gallerano *et al.* [2014].

The numerical integration of Eqs. (5) and (6) is carried out by a high resolution hybrid finite volume-finite difference scheme. The conservative part of the above equations, consisting of the convective terms and terms related to the free surface elevation, is discretized by a high-order shock-capturing finite volume upwind WENO scheme [Gallerano *et al.*, 2012]; dispersive terms and the terms related to the approximation to the second order of the vertical vorticity are discretized by a cell-centered finite difference scheme. The finite volume upwind WENO scheme needs a flux calculation at the cell interfaces. These fluxes are calculated by means of the solution of a Riemann problem. An exact Riemann solver is used in this work. The shock-capturing method makes it possible to intrinsically model the wave breaking, therefore no additional terms are needed to take into account the breaking related energy dissipation in the surf zone.

Coast. Eng. J. 2016.58. Downloaded from www.worldscientific.com
by UNIVERSITA DEGLI STUDI DI ROMA on 10/19/16. For personal use only.

2.1.1. *Undertow*

In the proposed model, the improvement of the undertow predictions is obtained by using the methodology proposed by Lynett [2006]. In particular, the modified instantaneous vertical profile of the contravariant component of the horizontal velocities $u^l(z,t)$ is given by

$$u^l(z,t) = u^l_\alpha(t) + (\sigma - z)g^{lm}[(hu^k_\alpha(t))_{,k}]_{,m} + [(\sigma^2/2) - (z^2/2)]g^{lm}[(u^k_\alpha(t))_{,k}]_{,m} + u^l_B(z,t), \quad (7)$$

where $u^l_\alpha(t)$ is the contravariant component of the horizontal velocity at an arbitrary distance from the still water level (which is calculated by the integration of Eqs. (5) and (6)), the second and the third term on the right-hand side of Eq. (14) represent the high-order terms in depth power expansion of the velocity and $u^l_B(zt)$ is the contravariant component of the corrective velocity proposed in Lynett [2006].

2.1.2. *Intra-wave hydrodynamic variables*

Phase resolving models for the simulation of the wave and current fields are able to provide the vertical profile of the instantaneous velocity, which is a direct sum of the oscillating and steady components.

In this paper, the variation during the wave period of the intra-wave hydrodynamic quantities is calculated following the conceptual line proposed by Fredsøe [1984] and integrating the momentum equation over the wave boundary layer. In the integration over the wave boundary layer of the above-mentioned equation, the velocity at the top of the wave boundary layer is instantly evaluated from the velocity values produced by the integration of Eqs. (5) and (6), taking into account the high-order terms in the depth power expansion of the velocity and the correction proposed by Lynett [2006] according to Eq. (7). The calculation of the intra-wave hydrodynamic variables is related to the value of the horizontal velocity that instantly takes into account the wave–current interaction and the vertical profile of the above horizontal velocities, including the undertow in the surf zone. Hence, the calculation procedure of the intra-wave hydrodynamic variables makes it possible to simulate the bed evolution dynamics even in random wave conditions, whose free surface elevation and velocity fields cannot be simulated using the potential theory.

Let $\delta(t)$ be the instantaneous wave boundary layer thickness, let $u_f(t)$ be the instantaneous value of the friction velocity and let $U(z,t)$ be the horizontal velocity magnitude defined in a Cartesian reference system at the generic height z inside the wave boundary layer. $U(z,t)$ is obtained from $u^l(z,t)$ (defined by Eq. (7)) through the use of the transformation relations (Eq. (3)). $U_\delta(t)$ is the instantaneous value of the horizontal velocity magnitude calculated at the top of the wave boundary layer.

Coast. Eng. J. 2016.58. Downloaded from www.worldscientific.com
by UNIVERSITA DEGLI STUDI DI ROMA on 10/19/16. For personal use only.

The logarithmic velocity profile inside the wave boundary layer is given by

$$\frac{U(z,t)}{u_f(t)} = \frac{1}{K}\ln\left(\frac{z}{\frac{k}{30}}\right), \tag{8}$$

where K is the von Karman constant (equal to 0.4) and k is the bed roughness equal to $2.5d_{50}$ with d_{50} the sediment mean diameter.

Equation (8), analytically integrated over z between the height $z = k/30$ from the bottom and the height $z = \delta(t)$, where the instantaneous horizontal velocity magnitude $U_\delta(t)$ is calculated, gives the following expression of the instantaneous wave boundary layer thickness $\delta(t)$

$$\delta(t) = \frac{k}{30}(e^{f(t)} - 1) \tag{9}$$

in which $f(t)$ is defined as the following dimensionless quantity

$$f(t) = \frac{U_\delta(t)}{u_f(t)}K. \tag{10}$$

The integration of the momentum equation over the wave boundary layer leads to

$$\int_{\frac{k}{30}}^{\delta(t)+\frac{k}{30}} \frac{\partial(U_\delta(t) - U(z,t))}{\partial t}dz = u_f^2(t). \tag{11}$$

By introducing Eqs. (8)–(10) into Eq. (11) the following equation, describing the time evolution of the friction velocity $u_f(t)$, is given

$$-u_f^2(t) = -\delta(t)\frac{dU_\delta(t)}{dt} + \frac{1}{K}\frac{du_f(t)}{dt}\frac{k}{30}[e^{f(t)}(f(t) - 1) + 1]. \tag{12}$$

The instantaneous value of $u_f(t)$ is obtained by numerically integrating Eq. (12). The time integration of the above equation is carried out by means of a third order accurate strong stability preserving Runge–Kutta (SSPRK) method reported in Spiteri and Ruuth [2002].

Thus, obtained, the value of $u_f(t)$, introduced in Eq. (10), gives the value of the dimensionless quantity $f(t)$. Such value of $f(t)$, introduced in Eq. (9), gives the value of the instantaneous wave boundary layer thickness $\delta(t)$.

The values of $f(t)$, $u_f(t)$ and $\delta(t)$ intervene in the description of the process whereby the sediment is brought into suspension and carried away from the bed because of the expansion of the boundary layer.

The instantaneous values of $u_f(t)$ and $\delta(t)$ are used to calculate the instantaneous values of the eddy viscosity, by means of the procedure shown below.

Let the mark $[\ \widetilde{}\ ]$ indicate the wave-averaged value of the generic instantaneous quantity and let T be the wave period.

Coast. Eng. J. 2016.58. Downloaded from www.worldscientific.com
by UNIVERSITA DEGLI STUDI DI ROMA on 10/19/16. For personal use only.

Under wave–current interaction, inside the wave boundary layer the turbulence structure is due to both the wave and the current, while outside the wave boundary layer it is due to the current only.

In conditions of wave–current interaction, inside the wave boundary layer the following eddy viscosity vertical distribution is assumed

$$\nu_{t,r}(z,t) = K u_f(t) z \left[1 - \frac{z}{\delta(t)}\left(1 - \frac{\widetilde{u_{fc}}}{u_f(t)}\right)\right]\left(1 - \frac{z}{\tilde{H}}\right), \tag{13}$$

where $\widetilde{u_{fc}}$ is the current friction velocity given by the following expression

$$\widetilde{u_{fc}}^2 = \frac{1}{T}\int_0^T u_f^2(t)dt \tag{14}$$

obtained from the integration (with respect to time) of the momentum equation over one wave period.

Outside the wave boundary layer, the eddy viscosity vertical distribution is assumed as

$$\nu_{t,r}(z) = \widetilde{u_{fc}} K z \left(1 - \frac{z}{\tilde{H}}\right). \tag{15}$$

At the top of the boundary layer, the eddy viscosity produced by Eq. (13) assumes the same value as the eddy viscosity produced by Eq. (15).

Instead, under breaking waves the main contribution to the turbulence structure in the proximity of the free surface is due to the wave breaking, which is in fact responsible for the production of turbulent kinetic energy. The turbulence produced by the wave breaking is added to the turbulence due to the wave boundary layer and current, and it increases the amount of sediment particle kept in suspension. The contribution of the wave breaking to the eddy viscosity distribution $\nu_{t,f}(z,t)$ is computed by instantly solving the transport equation for turbulent kinetic energy as presented by Deigaard *et al.* [1986]

$$\frac{\partial k_t}{\partial t} = \frac{\text{PRODU}}{\rho} - c_d \frac{k_t^{\frac{3}{2}}}{l} + \frac{\partial}{\partial z}\left(\frac{\nu_{t,f}(z,t)}{\sigma_k}\frac{\partial k_t}{\partial z}\right), \tag{16}$$

where $k_t = k_t(z,t)$ is the turbulent kinetic energy developed during the wave breaking; the first term on the right-hand side of Eq. (16) is the production of turbulent kinetic energy, the second and third term are, respectively, the dissipation and turbulent diffusion term. σ_k is the Prandt number for the diffusion (for incompressible fluids constant and equal to unity), $c_d = 0.08$ and l is the length scale of turbulence. In the above-mentioned equation, the kinetic energy is set to zero at the bottom and a null value of the normal derivative of the kinetic energy is set as boundary condition at the free surface. In Eq. (16), the horizontal diffusion terms are neglected, since in shallow water waves the horizontal length scale, represented by the wave

Coast. Eng. J. 2016.58. Downloaded from www.worldscientific.com
by UNIVERSITA DEGLI STUDI DI ROMA on 10/19/16. For personal use only.

length, is very large compared with the vertical length scale, represented by the water depth.

The turbulent kinetic energy production term appearing in Eq. (16) can be expressed, following Deigaard *et al.* [1986], in the form

$$\mathrm{PRODU} = E_{\mathrm{loss}} \frac{36}{\tilde{H}_w \beta_p T^2} \xi \left(1 - \frac{\xi}{\tilde{H}_w}\right) \cdot \mathrm{CSM}(t), \tag{17}$$

where E_{loss} is the kinetic energy loss during the hydraulic jump in the wave period, $\tilde{H}_w$ is the wave height, $\xi = -z$ is the generic depth with origin in correspondence with the free surface, β_p is the fraction of the wave period during which the production of turbulent kinetic energy takes place and $\mathrm{CSM}(t)$ is a coefficient that takes values between 0 and 1 taking into account the wave breaking phenomenon as a function of $\partial\eta/\partial t$ (similarly to what is proposed in Kennedy *et al.* [2000].

The instantaneous value of k_t is obtained by numerically integrating Eq. (16). The last term on the right-hand side of Eq. (16) is discretized along the z-direction by a second order finite difference scheme and the time integration of the above equation is carried out by means of a third-order accurate SSPRK method reported in Spiteri and Ruuth [2002].

The instantaneous value of k_t thus obtained is then inserted into the expression for the calculation of the eddy viscosity due only to wave breaking

$$\nu_{t,f}(z,t) = l\sqrt{k_t}. \tag{18}$$

Under wave breaking, the near-bottom turbulence is mainly related to the shear stress that develops inside the wave boundary layer, while moving toward the free surface, the turbulence is produced by the current and the wave breaking. Consequently the total eddy viscosity $\nu_t(z,t)$, produced by the wave–current interaction and the wave breaking, is the quadratic sum of the two components

$$\nu_t^2(z,t) = \nu_{t,r}^2(z,t) + \nu_{t,f}^2(z,t). \tag{19}$$

The calculation of the intra-wave hydrodynamic variables thus presented can be used whatever wave–current interaction occurs, even in those cases in which, with respect to the coastline, the wave-generated current is mostly parallel and the incident waves are nearly perpendicular.

2.2. *Morphodynamic model*

The morphodynamic model is based on the wave-averaged advection–diffusion equation for the suspended sediment concentration in which a Q3D approach is adopted for the advective sediment transport terms.

Coast. Eng. J. 2016.58. Downloaded from www.worldscientific.com
by UNIVERSITA DEGLI STUDI DI ROMA on 10/19/16. For personal use only.

The integral form of the above-mentioned equation in contravariant formulation is

$$\iint_{\Delta A} \frac{\partial \bar{\tilde{C}} \tilde{H}}{\partial t} dA + \int_L \left[\int_a^{\tilde{H}} \tilde{C}(z) \tilde{u}^m(z) dz \right] n_m dL - \int_L K_d \tilde{H} g^{ml} (\bar{\tilde{C}})_{,l} n_m dL = \iint_{\Delta A} (P - D) dA, \tag{20}$$

where L is the contour line of ΔA and n_m is the mth component of the covariant outward normal, K_d is given by the eddy viscosity, $\tilde{H}$ is the wave-averaged total water depth, $\tilde{u}^m(z)$ is the vertical distribution of the contravariant component of the horizontal velocity vector obtained averaging over a wave period the modified instantaneous vertical profile of the contravariant component of the horizontal velocity vector (calculated from the integration of the motion equations (5) and (6) and by Eq. (7) which take into account the high-order terms in depth power expansion of the velocity and the correction by Lynett [2006]) and $\tilde{C}(z)$ is the vertical distribution of the wave-averaged suspended sediment concentration. The point located at a distance a from the bottom (which is used as the lower limit of integration in Eq. (20)) separates the lower layer, where the sediment particles move by rolling, sliding, or in short jumps, from the upper layer where the sediment particles are held in suspension by turbulence: in the lower layer the bed load transport occurs, while in the upper layer the suspended load transport takes place.

The terms related to the line integral on the left-hand side of Eq. (20) are calculated starting from the depth integration of the product of the wave-averaged horizontal velocity vertical distribution and wave-averaged suspended sediment concentration vertical distribution (similarly to Jayaratne *et al.* [2014]), in order to take into account the sediment transport related to the undertow and the effects produced on the concentration by the eddy viscosity vertical distribution.

The source term D, which represents the sediment deposition rate, and the source term P, which represents the sediment pick-up rate, are defined in the following expressions:

$$D = w_{\text{sed}} \tilde{C}_a, \tag{21}$$

$$P = w_{\text{sed}} \tilde{C}_R, \tag{22}$$

where w_{sed} is the sediment fall velocity, $\tilde{C}_a$ is the actual concentration and $\tilde{C}_R$ is the reference concentration (both the concentration values are evaluated at reference height $a = 2d_{50}$).

The value of $\bar{\tilde{C}}$ is obtained by Eq. (20). The numerical integration of Eq. (20) is carried out by a high-order shock-capturing finite volume upwind WENO scheme [Gallerano *et al.*, 2012]. Such integration implies the calculation at each time instant of $\tilde{C}_a$ and of $\tilde{C}(z)$.

Coast. Eng. J. 2016.58. Downloaded from www.worldscientific.com
by UNIVERSITA DEGLI STUDI DI ROMA on 10/19/16. For personal use only.

Coast. Eng. J. 2016.58. Downloaded from www.worldscientific.com
by UNIVERSITA DEGLI STUDI DI ROMA on 10/19/16. For personal use only.

The value of the actual concentration $\tilde{C}_a$, which appears in Eq. (21), depends on the vertical distribution of the wave-averaged suspended sediment concentration $\tilde{C}(z)$. Under wave–current interaction and nonbreaking waves, the suspended sediment concentration is determined by the turbulence due to the wave and current. In the case at weak current, the vertical distribution of the suspended sediment concentration is mainly due to the wave-induced turbulence (which is near-bed confined) and, as a consequence, the above-mentioned concentration will be greater in the proximity of the bottom. In the case in which the current-induced turbulence is dominant compared to the wave-induced turbulence, the suspended sediment concentration will have a more uniform distribution over the water column. Under breaking waves, the vertical distribution of the suspended sediment concentration is mainly due to the turbulence induced by wave breaking and, consequently, the above-mentioned concentration will be greater in the proximity of the free surface (with respect to nonbreaking waves). The $\tilde{C}(z)$ depends on the wave-averaged total eddy viscosity $\tilde{\nu}_t(z)$ (calculated by averaging the value of the total eddy viscosity obtained from Eq. (19) over a wave period).

The value of the actual concentration $\tilde{C}_a$ must satisfy, as a lower boundary condition, the steady diffusion equation [Jayaratne and Shibayama, 2007]

$$-\tilde{C}(z)w_{\text{sed}} = \tilde{\nu}_t(z)\frac{\partial \tilde{C}(z)}{\partial z} \tag{23}$$

and must satisfy, as a lower extreme of integration, the integral

$$\bar{\tilde{C}} = \frac{1}{\tilde{H}}\int_a^{\tilde{H}} \tilde{C}(z)dz. \tag{24}$$

The calculation of $\tilde{C}_a$ and $\tilde{C}(z)$, which intervenes in the second term on the left-hand side of Eq. (20), is performed by means of an iterative procedure, starting from the values of $\bar{\tilde{C}}$ and $\tilde{\nu}_t(z)$, as shown in Appendix B.

The reference concentration $\tilde{C}_R$ is calculated starting from its instantaneous values $C_R(t)$ according to the expression proposed by Zyserman and Fredsøe [1994] and used by Rakha *et al.* [1997]

$$C_R(t) = \frac{0.331(|\vec{\theta}| - \theta_{\text{cr}})^{1,75}}{1 + \frac{0.331}{C_m}(|\vec{\theta}| - \theta_{\text{cr}})^{1,75}}, \tag{25}$$

where C_m is the maximum volumetric concentration achievable on the water column, θ_{cr} is the Shield stability parameter i.e. the critical dimensionless bed shear stress (which is only a function of the physical characteristics of the bed material as defined by Van Rijn [1984a]) and $|\vec{\theta}| = |\vec{\theta}(t)|$ is the Shield mobility parameter defined as the modulus of vector $\vec{\theta}(t)$, i.e. the instantaneous dimensionless bed shear stress produced by the combined wave–current action. Such Shield mobility parameter is

a function of the friction velocity $u_f(t)$, according to the expression

$$\vec{\theta}(t) = \frac{u_f(t)^2}{(s_{\text{rel}} - 1)Gd_{50}} \cdot \frac{\vec{u}_a}{|\vec{u}_a|}, \tag{26}$$

where s_{rel} is the relative density of the sediment and $\vec{u}_a$ is the instantaneous horizontal velocity vector (expressed in a Cartesian system of reference) calculated at distance a from the bottom; the contravariant components of vector $\vec{u}_a$ are given by Eq. (7).

For the calculation of the bed load transport, the Engelund and Fredsøe [1976] formula is used. The wave-averaged bed load transport vector $\tilde{\vec{q}}_b$ is calculated by means of the following expression:

$$\tilde{\vec{q}}_b = \frac{1}{T}\int_0^T \left(5\left(1 + \left(\frac{\frac{\pi}{6}\beta}{|\vec{\theta}| - \theta_{\text{cr}}}\right)\right)^{-1/4} \cdot (\sqrt{|\vec{\theta}|} - 0.7\sqrt{\theta}_{\text{cr}})\sqrt{(s_{\text{rel}} - 1)Gd_{50}^3}\right) \cdot \frac{\vec{u}_a}{|\vec{u}_a|} dt \tag{27}$$

where β is the dynamic friction coefficient that is the tangent of the dynamic friction angle for the bed load sediment. For random waves, $\tilde{\vec{q}}_b$ represents the wave-averaged value over several wave cycles. It must be noted that this formula defines the bed load as the sediment particles in the lowest layer of moving grains.

In this paper, the boundary of the computational domain for the numerical integration of the advection–diffusion equation for the suspended sediment concentration is placed at the border between the inner surf zone and the swash zone at the location of the start of the uprush. Thus, it is necessary to impose a boundary condition for this equation that represents the contribution provided by the swash zone to the transported material in the surf zone. In order to obtain this boundary value, we follow the approach proposed by Nam *et al.* [2009]. According to this approach, the sediment transport at the location of the start of the uprush obtained from the swash zone computations is used as the boundary value for the numerical solution of the advection–diffusion equation for the suspended sediment concentration. Similarly to Nam *et al.* [2009], we calculate the net sediment transport from the swash zone from the Larson and Wamsley [2007] expressions, which provide the net amount of sediment that is exchanged, at the end of every swash cycle (uprush–backwash cycle), between the swash and the inner surf zone.

Let the uprush boundary be the line made of the points that identify the start of the uprush (and which separates the swash zone from the inner surf zone). For random waves, the uprush boundary is calculated as the mean value, over several wave cycles, of the locations of the start of the uprush related to each single swash cycle.

Let us define, in each point of the line which identifies the uprush boundary, a local Cartesian system of reference with coordinates x^*, y^*, in which the x^*-axis is offshore-directed along the line of maximum slope.

Coast. Eng. J. 2016.58. Downloaded from www.worldscientific.com
by UNIVERSITA DEGLI STUDI DI ROMA on 10/19/16. For personal use only.

For each swash cycle we indicate with $\vec{q}_{b\,\mathrm{net}}$ the net sediment transport vector averaged over the whole swash cycle calculated at the origin of the above-mentioned local Cartesian reference system. The components of the $\vec{q}_{b\,\mathrm{net}}$ vector, according to the above-mentioned Larson and Wamsley [2007] formula, are given by

$$q_{b\,\mathrm{net}_{x^*}} = K_{x^*} \frac{\tan \Phi_m}{\tan^2 \Phi_m - (dh/dx^*)^2} \frac{u_0^3}{g} (dh/dx^* - \tan \beta_e), \tag{28}$$

$$q_{b\,\mathrm{net}_{y^*}} = K_{y^*} \frac{\tan \Phi_m}{\tan^2 \Phi_m - (dh/dx^*)^2} \frac{u_0^2 v_0}{g}, \tag{29}$$

where K_{x^*} and K_{y^*} are empirical coefficients, Φ_m is the friction angle for a moving grain, β_e is the foreshore equilibrium slope, dh/dx^* is the foreshore slope, u_0 and v_0 are the scalar components of vector $\vec{u}_0$ in the local Cartesian reference system. In Eqs. (28) and (29), vector $\vec{u}_0$ is defined as a scaling velocity whose values are assumed to be equal to the propagation velocity of the wet and dry front at the start of the uprush (consistently with Larson *et al.* [2004] that define $\vec{u}_0$ as the bore front velocity).

In order to calculate $\vec{u}_0$, a new procedure for the simulation of the uprush and backwash dynamics of the wet and dry front is used. The values of $\vec{u}_0$ are obtained from the solution of the exact wet and dry Riemann problem defined by the hyperbolic homogeneous system of the shallow water equations written in the locally valid ortho-normal basis. The exact wet and dry Riemann problem is included in an asymmetric upwind-WENO numerical procedure.

Under random waves, the value of $\vec{u}_0$ is calculated as the mean value over several swash cycles of the propagation velocity of the wet and dry front related to each single swash cycle.

The net sediment transport from the swash zone calculated at the uprush boundary acts as a boundary condition in the wave-averaged advection–diffusion equation for the suspended sediment concentration (Eq. (20)), in order to take into account the interaction between the swash zone and the inner part of the surf zone.

The numerical integration of Eq. (20) is carried out by the high-order upwind WENO finite volume scheme proposed to solve the motion equations in the hydrodynamic model.

Once the values of the reference concentration and the actual concentration are known, the suspended load is calculated by the difference $(P - D)$ between the sediment pick-up rate and the sediment deposition rate. Such difference is inserted into the following bed change equation

$$\frac{\partial z_f}{\partial t} = -\frac{1}{1-p}[(P - D) + \tilde{q}_{b,l}^l], \tag{30}$$

where z_f is the bed elevation, p is the sediment porosity and $\tilde{q}_b^l (l = 1, 2)$ is the contravariant component (in a curvilinear system of coordinates) of the wave-averaged

Coast. Eng. J. 2016.58. Downloaded from www.worldscientific.com
by UNIVERSITA DEGLI STUDI DI ROMA on 10/19/16. For personal use only.

bed load transport vector $\tilde{\vec{q}}_b$. This equation is solved in the portion of the domain from deep water up to the seaward end of the swash zone (uprush boundary).

In the swash zone, the bed changes are calculated by means of the following equation:

$$\frac{\partial z_f}{\partial t} = -\frac{1}{1-p} q^l_{S,l}, \tag{31}$$

where $q^l_{S,l}$ is the contravariant component of the vector $\vec{q}_S$ which represents the wave-averaged net sediment transport vector (over the swash cycle) at each point of the line of maximum slope which is inside the swash zone and defined in the above local Cartesian reference system.

The variability along x^*-axis of the components of the above-mentioned vector is given in the following form:

$$q_{S_{x^*}}(x^*) = K_{x^*} \frac{\tan \Phi_m}{\tan^2 \Phi_m - (dh/dx)^2} \frac{u^3_{0S}}{g} (dh/dx^* - \tan \beta_e) \frac{t_o}{T}, \tag{32}$$

$$q_{S_{y^*}}(x^*) = K_{y^*} \frac{\tan \Phi_m}{\tan^2 \Phi_m - (dh/dx^*)^2} \frac{u^2_{0S} v_{0S}}{g} \frac{t_o}{T}, \tag{33}$$

where t_0 is the duration of the swash at the abscissa x^* of the above-mentioned local Cartesian reference system, T is the duration of the swash cycle, u_{0S} and v_{0S} are the scalar components of the propagation velocity vector of the wet and dry front $\vec{u}_{0S}$, obtained from the solution of the exact wet and dry Riemann problem, at abscissa x^* into the swash zone. Under random waves, the value of $\vec{u}_{0S}$ is calculated, in correspondence with x^*, as the mean value over several wave cycles of the propagation velocity of the wet and dry front related to each single swash cycle. The above-mentioned calculation of the propagation velocity vector $\vec{u}_{0S}$ is consistent with the approach proposed in Larson *et al.* [2004], where $\vec{u}_{0S}$ is taken as the velocity that the bore front assumes, at the particular location x^*, in the uprush phase of this swash cycle and is defined as a scaling velocity which characterizes the net sediment transport obtained from the difference between the mean sediment transport over the uprush phase that starts at x^* and the mean sediment transport over the backwash phase that ends at the same abscissa x^*.

It must be noted that Eqs. (32) and (33) reduce to Eqs. (28) and (29) when x^* is set to zero and consequently t_0 coincides with T and $\vec{u}_{0S}$ coincides with $\vec{u}_0$.

2.2.1. *Hydrodynamic–Morphodynamic coupling*

The hydrodynamic model and the morphodynamic model are used for the simulation of long-term bed evolution dynamics.

The computation of the long-term bed evolution is carried out by a sequence that alternates the simulation of wave and current velocity fields and the simulation of the sediment transport and bed morphological change. The procedure, whereby

Coast. Eng. J. 2016.58. Downloaded from www.worldscientific.com
by UNIVERSITA DEGLI STUDI DI ROMA on 10/19/16. For personal use only.

the coupling between the two models is realized, can be schematized by a sequence of four steps described below.

The completion of a whole sequence of the four steps, that compose the above procedure, corresponds to the completion of a so-called "morphological step". At each morphological step, the following computations are performed:

(1) Starting from an initial bathymetry, the hydrodynamic model calculates the instantaneous values of the free surface elevation, vertical distribution of horizontal velocities, vertical distribution of the eddy viscosity, wave boundary layer thickness, friction velocity and reference concentration; these values are calculated by integrating the Boussinesq equation (Eqs. (5) and (6)), on a fixed bathymetry, with input values of the wave motion forces such as to reproduce a storm event. According to the approach proposed by Rakha *et al.* [1997], the hydrodynamic model does not run in the real-world time but in a simulation time that, at each morphological step, (for random waves) has a duration of about 100–150 times the mean wave period.
(2) The instantaneous values of the hydrodynamic quantities (calculated with the Boussinesq model) are averaged over a time interval of 100–150 times the mean wave period. Thus obtained the values are called wave-averaged values.
(3) The wave-averaged values are used as input to the wave-averaged advection–diffusion equation for the suspended sediment concentration, expressed by Eq. (20) which is numerically integrated with a time discretization step that is the same as the one used in the hydrodynamic model. The time integration of Eq. (20) is carried out until a stationary state is reached for the suspended sediment concentration. The values of $\tilde{C}_a$, which represents the wave-averaged value of the actual concentration at a distance a from the bottom, are obtained from the depth and wave-averaged concentration values $\bar{\tilde{C}}$.
(4) The wave-averaged actual concentration $\tilde{C}_a$ and the wave-averaged bed load transport $\vec{\tilde{q}}_b$ intervene (together with the wave-averaged reference concentration $\tilde{C}_R$) in the integration of the bed change equation, Eq. (30), which makes it possible to update the bathymetry for the next morphological step. Equation (30) is integrated over a simulation time interval greater than the one during which the Boussinesq model runs. The duration of the simulation time interval over which Eq. (30) is integrated is called "morphological time step".

Once the bed elevations are updated, the whole sequence, consisting of the four steps previously described, is repeated to carry out the next morphological step.

A flow chart of the above-mentioned computational procedure is shown in Fig. 1.

3. Results

In this section, the proposed model for the simulation of the bed evolution dynamics is verified against a set of test cases.

Coast. Eng. J. 2016.58. Downloaded from www.worldscientific.com
by UNIVERSITA DEGLI STUDI DI ROMA on 10/19/16. For personal use only.

Coast. Eng. J. 2016.58. Downloaded from www.worldscientific.com
by UNIVERSITA DEGLI STUDI DI ROMA on 10/19/16. For personal use only.

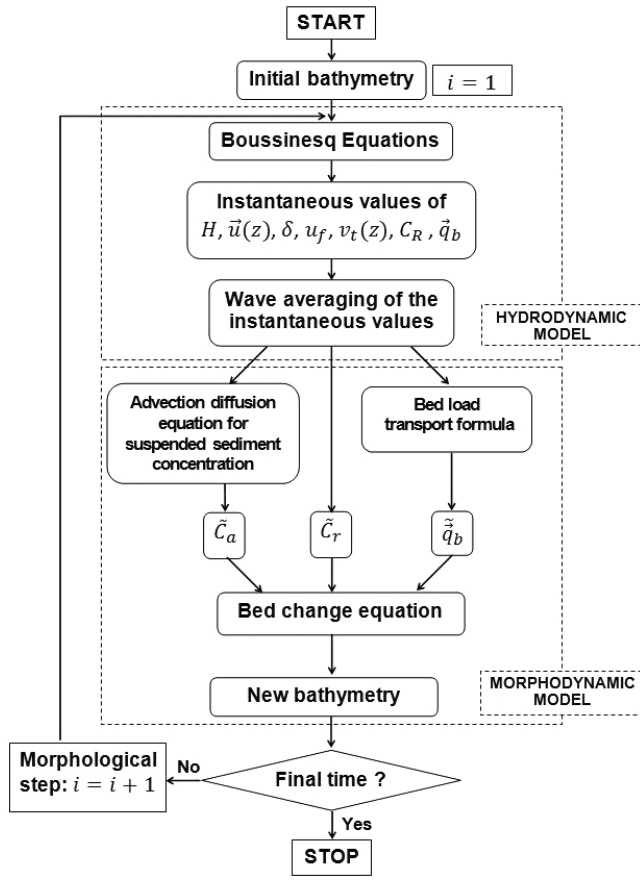

Fig. 1. Flow chart of the computational procedure.

3.1. *Sandbar formation*

Two experiments (Test 1a and 1b) extracted from "LIP 11D Delta Flume Experiments", described in the data report by Roelvink and Reniers [1995], are numerically reproduced. The report contains hydrodynamic and sediment transport measures.

The experiments were conducted in a wave flume with a 183-m long mobile bottom and were carried out so as to reproduce slightly erosive wave conditions (Test 1a) acting for 12 h, and highly erosive wave conditions (Test 1b) acting for 18 h. In both tests, narrow-banded random waves were generated (by a random-phase, linear generator from a JONSWAP spectrum) at $X = 0$ m normally incident to the coast, whose characteristics are shown in Table 1.

In Fig. 2, the beach profile representing the bottom of the wave flume used as initial condition and the still water level for Test 1a are shown. The wave flume was characterized by an initial region of water depth 4.1 m, an intermediate region of varying water depth which follows a Dean-type bottom profile (the so-called equilibrium beach parabolic profile of Brunn–Dean–More) and a final region of

Table 1. Incident wave characteristics for Test 1a and 1b.

Test code	Hm_0 (m)	T_p (s)	Water level (m)	Duration (h)
la	0.9	5	4.1	12
1b	1.4	5	4.1	18

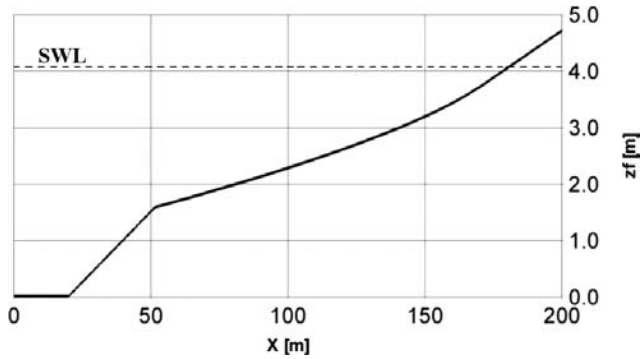

Fig. 2. Initial bottom profile (black line) and still water level (dashed black line) for Test 1a.

Coast. Eng. J. 2016.58. Downloaded from www.worldscientific.com
by UNIVERSITA DEGLI STUDI DI ROMA on 10/19/16. For personal use only.

varying water depth which follows a constant bottom slope. The initial position of the shoreline is approximately located at $X = 181\,\text{m}$. In the experiment, the sediment was characterized by a mean diameter of $220\,\mu\text{m}$.

Test 1a and 1b are both numerically reproduced by internally generating random wave trains, characterized by a JONSWAP frequency spectrum with a significant wave height respectively of 0.9 m and 1.4 m. The computational grid is one-dimensional and has a spatial discretization of $\Delta x = 0.3\,\text{m}$. The time discretization step for the phase-resolving hydrodynamic model is 0.01 s.

The simulation of the bed morphological change is performed by using a sequence of 120 morphological steps for Test 1a and 180 morphological steps for Test 1b, in which each morphological step corresponds to a bed morphological change over a time interval of 0.1 h (morphological time step). Each morphological step requires the consecutive application of the numerical models described in Sec. 2.

In Figs. 3(a) and 3(b) the comparison between the values of the averaged total sediment transport obtained at the end of the numerical simulation (black line) and those experimentally measured (red line), respectively for Test 1a and Test 1b, are shown.

As can be seen from Fig. 3(a), the wave-averaged total sediment transport calculated for Test 1a assumes almost null values in the deep water region while it attains significant values in two regions of the computational domain. The first region is located around $X = 145\,\text{m}$, corresponding to where the wave breaking starts and so where sediment resuspension phenomena are larger. From the above figure it is noted that, in this region the wave-averaged total sediment transport is offshore directed. The second region is located around $X = 170\,\text{m}$; in this region the

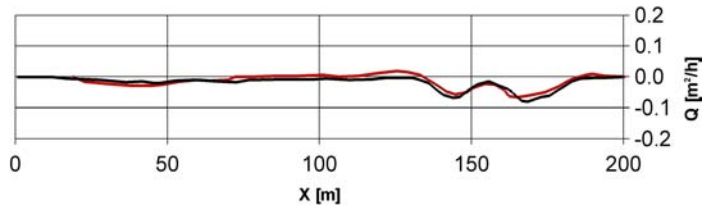

(a)

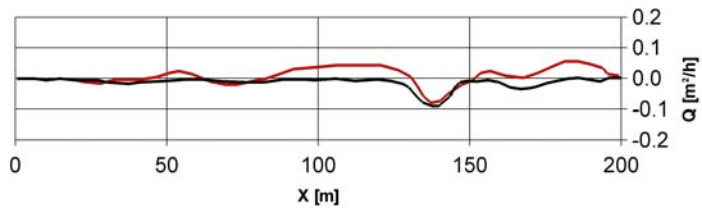

(b)

Fig. 3. Comparison of calculated (black line) and measured (red line) wave-averaged total sediment transport for Test 1a (a) and Test 1b (b) by using the proposed model.

Coast. Eng. J. 2016.58. Downloaded from www.worldscientific.com
by UNIVERSITA DEGLI STUDI DI ROMA on 10/19/16. For personal use only.

wave-averaged total sediment transport is represented by the sediment contribution provided by the swash zone. Even in the above-mentioned region, the wave-averaged total sediment transport is offshore directed.

Analogous considerations about the computed wave-averaged total sediment transport for Test 1a could be made also for Test 1b. As can be observed from Fig. 3(b), the most significant values of the computed wave-averaged total sediment transport are reached around $X = 137\,\mathrm{m}$, where the wave breaks since, as shown below, the sandbar crest formed at the end of Test 1a is located in this region. Even in this case, the wave-averaged total sediment transport is offshore directed.

It must be noted that for both Test 1a and 1b, the bed load transport contribution to the wave-averaged total sediment transport calculated by means of the proposed model turns out to be less than the suspended sediment transport contribution (such result is further consistent with Rakha *et al.* [1997]).

In fact, in our model, the point that separates the two regions, characterized respectively by the suspended sediment transport and the bed load transport, is placed near the bed and is less then $2.5d_{50}$ from this: consequently in the adopted scheme, according to the conceptual line by Engelund and Fredsøe [1976], the thickness of the lower region characterized by the bed load (i.e. by the sediment particles moving by rolling, sliding, or in short jumps) is particularly small. In the upper region, sediment particles are held in suspension by turbulence. Since in Test 1a and 1b the sediment consists of very fine sand, the strong turbulence induced by waves tends to put into suspension most of the sediment and therefore the bed load transport is small for both Tests.

Coast. Eng. J. 2016.58. Downloaded from www.worldscientific.com
by UNIVERSITA DEGLI STUDI DI ROMA on 10/19/16. For personal use only.

The numerical results are overall in good agreement with the experimental data and show how the proposed model is both able to capture the sediment resuspension phenomena produced by wave breaking and the offshore sediment transport due to undertow currents.

In the specific case, an offshore sediment transport occurs since the breaking wave has a strong asymmetric shape, with higher bed shear stress under the crest and lower bed shear stress under the trough. This type of waves with a high ratio between height and length (as those reproduced in Test 1a and 1b) show a short and high wave crest (very steep front face), during which a strong turbulence develops, followed by a broad and flat wave trough. Under the crest, the instantaneous horizontal flow velocities are shoreward directed; as a consequence, under the crest, the transport of sediment held in suspension by turbulence is directed toward the shore.

Under the trough, in conditions of strongly asymmetric waves once again, the instantaneous horizontal velocities are offshore directed and the turbulence (powerfully produced by the wave breaking and not yet dissipated) is still able to keep the sediment in suspension. For these waves, that induce significant undertow currents, the sediment transport related to the trough phase is dominant with respect to that related to the crest phase and consequently the wave-averaged suspended sediment transport is offshore directed.

Figure 4(a) shows the bed changes, in respect to the initial configuration (shown in Fig. 2), obtained at the end of the simulation of Test 1a; Fig. 4(b) shows the bed changes, in respect to the final configuration of Test 1a, obtained at the end of the simulation of Test 1b.

The numerical results presented in Fig. 4(a) reveal the presence of two sandbars in the nearshore zone: the first is formed in the breaker zone and the second first is formed in the nearer area to the swash zone.

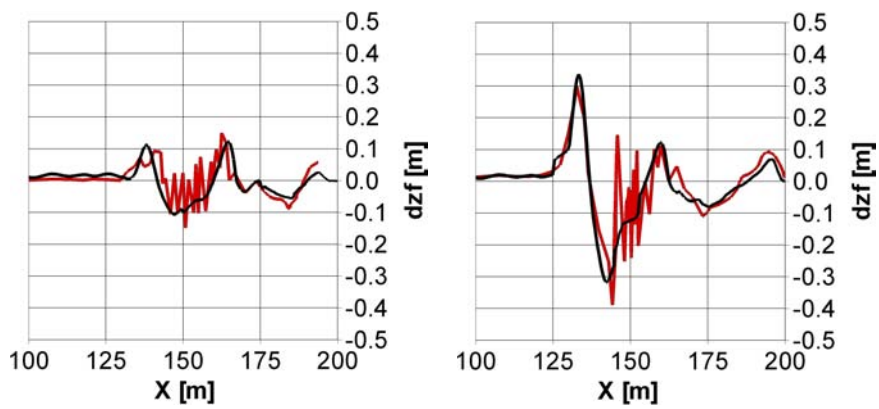

(a) (b)

Fig. 4. Comparison of calculated (black line) and measured (red line) bed changes for Test 1a (a) and Test 1b (b) by using the proposed model.

The first sandbar is located around at $X = 137\,\text{m}$ and is characterized by a crest height of 0.1 m about. The above-mentioned bar is produced by the deposit of sediment put into suspension in correspondence of the wave breaking ($145\,\text{m} < X < 155\,\text{m}$) and transported by undertow currents: such suspended sediment is bound to settle just seaward of the breaker zone due to a strong turbulence reduction.

The second sandbar is located around at $X = 165\,\text{m}$ and is characterized by a crest height of about 0.12 m. Such bed accretion is mainly due to the contribution to transported material from the swash zone.

The analysis of the numerical results, which globally agree with the experimental measurements, offers the chance to give a qualitative description of the sediment transport phenomena that drive the bar migration dynamics. In fact, the numerical results presented in Fig. 4(b) show a 7-m seaward migration for both the aforementioned sandbars. In particular, the first sandbar shows an height increase of 0.2 m about (respect to Test 1a), instead the second sandbar height is almost the same.

Furthermore, it is observed that the breaker zone, in Test 1b, is located in proximity of the first sandbar shown in Fig. 4(a) and developed starting from the initial bottom (Fig. 2) by the wave motion in Test 1a: the sediment that forms the above sandbar is again put into suspension by the wave breaking. The suspended sediment is then offshore transported, even in this case, by the undertow currents. Such sediment load is bound to settle, analogously to Test 1a, just seaward of the breaker zone due to a strong turbulence reduction.

A similar seaward sandbar migration dynamics involves the movement of the second sandbar located in the nearer area to the swash zone.

The numerical results are in good agreement with the experimental data in all sections of the wave flume, including the nearest area to shoreline; the proposed model predict reasonably well the bar migration and the general trends of the beach profile changes.

The agreement between the numerical results and the experimental data shows that, in order to be able to simulate the formation of bars in the surf zone, it is essential to develop models capable of:

- predicting the undertow, so taking into account the near-bed flow velocity responsible for the offshore sediment transport;
- taking into account the time variability of the intra-wave hydrodynamic quantities, in order to effectively represent the complexity of turbulent phenomena responsible for the bed material resuspension from the bottom upwards;
- simulating the run-up and run-down in the swash zone by a wet and dry scheme, in order to properly evaluate the flow velocities responsible for the offshore-directed sediment transport from this area;
- using a Q3D approach for the advective sediment transport terms, able to take into account the cross-shore suspended sediment transport due to the undertow;

Coast. Eng. J. 2016.58. Downloaded from www.worldscientific.com
by UNIVERSITA DEGLI STUDI DI ROMA on 10/19/16. For personal use only.

- taking into account the contribution provided from the swash zone to transported material;
- taking into account the contribution from the bed load transport to the total load.

3.2. *Bed evolution dynamics in proximity of coastal structures*

Test T3C1 extracted from "LSTF Experiments Transport by Waves and Currents & Tombolo Development Behind Headland Structures", described in the data report by Gravens and Wang [2007], is numerically reproduced.

That Test was carried out experimentally on a natural beach with a 4-m long T-head groin centrally located in the alongshore direction of the model beach and with head section parallel-positioned 4 m offshore of the initial shoreline. It had a duration of 184 min. The wave generators were programmed to generate a random wave characterized by a 0.26 m significant breaking wave height, 1.5 s period and an approximate wave angle of 6.5° with respect to the shoreline. In the experiment, the sediment were characterized by a mean diameter of 150 μm.

Test T3C1 is numerically reproduced by internally generating random wave trains characterized by a JONSWAP frequency spectrum and a significant breaking wave height of 0.26 m.

The rectangular computational domain used for Test T3C1 is shown in Fig. 5. The Cartesian computational grid has a spatial discretization of $\Delta y = 0.045$ m in the wave propagation direction and of $\Delta x = 0.06$ m in the direction perpendicular to the wave propagation.

The border of the laboratory basin used by Gravens and Wang [2007] to perform Test T3C1 are sketched by a dashed red line. In our work, in order to numerically reproduce the above-mentioned laboratory conditions, on the upper boundary of the computational domain (line I–L of Fig. 5) random wave trains are internally generated with a straight front parallel to the boundary. In Fig. 5, the 0.7-m bathymetry indicates the line over which the deep water region characterized by a constant depth is found; the 0-m bathymetry indicates the shoreline position.

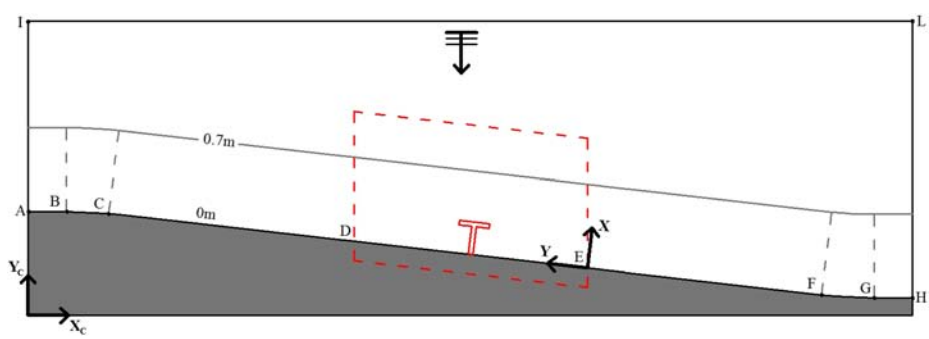

Fig. 5. Test T3C1. Computational domain for the hydrodynamic and morphodynamic model (solid black line); contours of the laboratory basin (dashed red line); T-head groin (solid red line).

Coast. Eng. J. 2016.58. Downloaded from www.worldscientific.com
by UNIVERSITA DEGLI STUDI DI ROMA on 10/19/16. For personal use only.

In the two regions included between the dashed lines identified by A–B and G–H, the shoreline and the bathymetric lines are perpendicular to the lateral boundaries of the computational domain: in this area the random wave fronts remain orthogonal to the lateral boundaries at every instant of time. Hence, the null value of the normal derivative of the instantaneous velocity and free surface elevation is set at the above-mentioned boundaries. Concerning the other boundaries, in correspondence with the sandy beach, a wet and dry technique is used, instead reflective boundary conditions are used over the boundaries affected by structures. In order to avoid reflections from the boundary located upstream the generation zone, a dissipation zone (sponge zone) is introduced into this area.

The stretch of coast D–E, where the T-head groin is centrally located, is sufficiently far from the lateral boundaries of the computational domain and from points C and F in Fig. 5. In this way, under the numerically generated wave motion force, in correspondence with the dashed lines indicated by D and E (that are sufficiently far from both points C and F and from the T-head groin), the depth and wave-averaged longshore current velocities are almost constant along the trajectories. The above-mentioned hydrodynamic conditions (that occur at the dashed lines marked by D and E) reproduce, with good approximation, the laboratory conditions in which Test T3C1 has been realized.

The equations of the morphodynamic model are integrated on the same computational domain and using the same Cartesian grid adopted for the hydrodynamic model.

At the lateral boundaries of the computational domain, the instantaneous and the wave-averaged values of the hydrodynamic quantities are almost constant along the normal to the border. Consequently, at these boundaries the wave-averaged bed load transport and the wave-averaged suspended sediment concentration are constant along the normal to the border. Null normal derivative of the wave-averaged suspended sediment concentration and wave-averaged bed load transport are assigned as lateral boundary conditions.

Concerning the other boundaries, in the stretch of coast characterized by a sandy beach, the boundary of the computational domain for the numerical integration of the advection–diffusion equation for the suspended sediment concentration is placed at the border between the inner surf zone and the swash zone, at the location of the start of the uprush. Over this boundary, the sediment transport obtained from the swash zone computation is used as the boundary value for the numerical solution of the above-mentioned equation (as described in Sec. 2.2). In the stretch of coast affected by structures, a null sediment flux at the boundary is imposed.

Let depth contour line be the line where the distance between the still water level and the bottom is constant and let bed elevation be the distance between the bottom and a fixed horizontal reference plane.

Figure 6 illustrates the computational grid and the depth contour lines in the initial condition for Test T3C1, and the two sections where experimental data are

Coast. Eng. J. 2016.58. Downloaded from www.worldscientific.com
by UNIVERSITA DEGLI STUDI DI ROMA on 10/19/16. For personal use only.

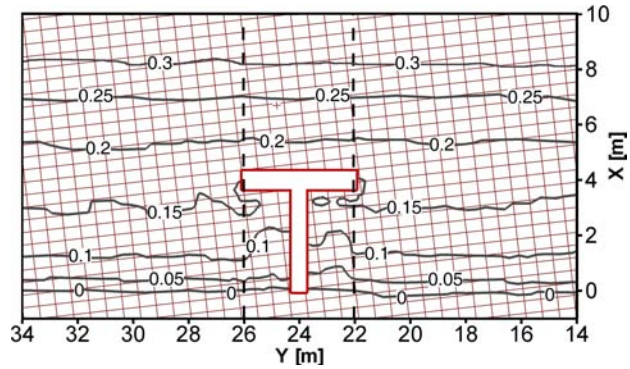

Fig. 6. Initial depth contour lines (gray solid lines), computational grid (red lines) and comparison sections (dashed lines) for Test T3C1.

Coast. Eng. J. 2016.58. Downloaded from www.worldscientific.com
by UNIVERSITA DEGLI STUDI DI ROMA on 10/19/16. For personal use only.

known. The time discretization step for the 2DPR hydrodynamic model is 0.0058 s which corresponds to a Courant–Friedrich–Lewy number of about 0.5. The simulation of the bed morphological change is performed by using a sequence of 180 morphological steps. Each morphological step corresponds to a bed morphological change over a time interval equal to 60 s (morphological time step) and requires the consecutive application of the numerical models described in Sec. 2.

In Fig. 7, an instantaneous wave field obtained by the numerical simulation of Test T3C1 carried out by the proposed model is shown. It is observed that, starting from about $X = 15$ m toward the shoreline the wave height gradually decreases because of the breaking. In the same figure it is noted that, in the lee of the T-head

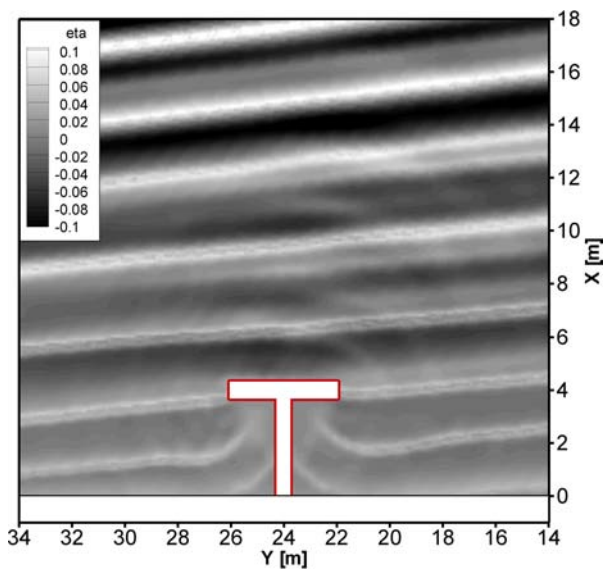

Fig. 7. Instantaneous wave field for Test T3C1.

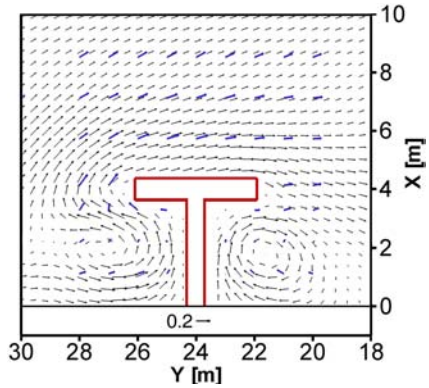

Fig. 8. Wave-averaged velocity field: calculated (black vectors) and measured (blue vectors) velocity current for Test T3C1.

Coast. Eng. J. 2016.58. Downloaded from www.worldscientific.com
by UNIVERSITÀ DEGLI STUDI DI ROMA on 10/19/16. For personal use only.

groin, the wave fronts, although attenuated by breaking, undergo a rotation owing to the diffraction effects.

In Fig. 8, the wave-averaged velocity field obtained by the numerical simulation of Test T3C1 carried out by the proposed model is shown. Figure 8 reveals the presence of a decreasing Y-directed longshore current in correspondence with the area between $X = 10\,\text{m}$ and the shoreline itself. In the figure, it can be seen that the current is intercepted and offshore-diverted by the T-head groin. Furthermore, the simulated velocity field is characterized by the formation of two eddies close to the T-head groin whose centers are well located. From Fig. 8, it can be seen that the wave-averaged velocity field, obtained by numerical simulation, is overall in good agreement with the experimental measurements.

Figure 9 shows the comparison between the simulated significant wave height and the corresponding experimental measurements by Gravens and Wang [2007] at the two sections ($Y = 26\,\text{m}$, $Y = 22\,\text{m}$), indicated in Fig. 6, that intersect the T-head groin. As can be seen in Figs. 9(a) and 9(b), the numerical results show a decay in wave height (produced by wave breaking) between about the abscissa $X = 14\,\text{m}$ and $X = 12\,\text{m}$, where the waves, coming from deep water regions, are affected by the sharp rise in the bed elevation. Approaching the shoreline, wave height almost does not modify from $X = 12\,\text{m}$ up to about $X = 4\,\text{m}$, where wave breaking ceases because the bed elevation is approximately constant. The numerical results reveal also a strong reduction of the wave height in the region between the head section of the T-groin and the shoreline ($X < 4\,\text{m}$) where the structure produce the maximum shielding effect on the incident waves. This figures shows that the numerical results are in good agreement with the experimental data.

Figure 10 presents the comparison between the simulated values of the longshore current and those experimentally measured by Gravens and Wang [2007] at the two sections previously indicated. The numerical results agree in general well with the experimental data. From Fig. 10(a) it is observed that near of the head section

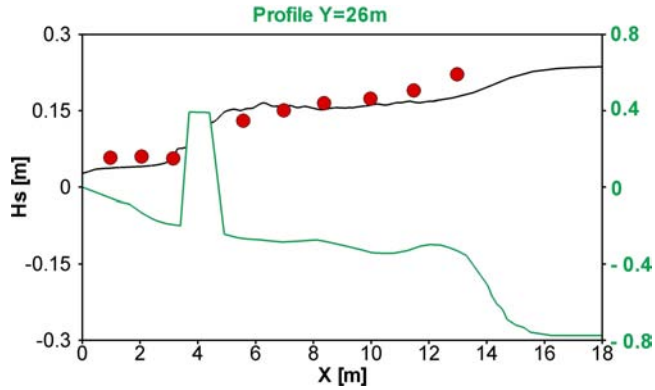

(a)

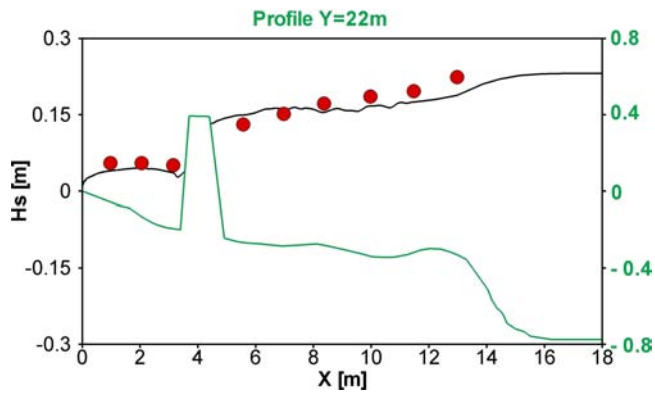

(b)

Fig. 9. Comparison of calculated (black lines) and measured (circles) significant wave height for Test T3C1 (beach profile in green line).

Coast. Eng. J. 2016.58. Downloaded from www.worldscientific.com
by UNIVERSITA DEGLI STUDI DI ROMA on 10/19/16. For personal use only.

downdrift side ($2\,\text{m} < X < 4\,\text{m}$) the numerical results show negative values of the current velocities due to the presence of a small eddy. The numerical results also show a small overestimation, compared to the experimental data, of the current velocity values in the region between $X = 2\,\text{m}$ and the shoreline. A similar pattern result is observed in Fig. 10(b) for $X < 4\,\text{m}$ where the longshore currents undergo an inversion in the closest area to the shoreline ($X < 2\,\text{m}$) due to the presence of a second eddy.

Figure 11 presents the comparison between the cross-shore current simulated values and those experimentally measured by Gravens and Wang [2007] at the two sections previously described. In these figures, it is observed that the numerical results are in good agreement with the experimental data.

In Fig. 12, the depth contour lines obtained at the end of the numerical simulation of Test T3C1 carried out by the proposed model (blue line), and the corresponding depth contour lines obtained from experimental data by Gravens and Wang [2007]

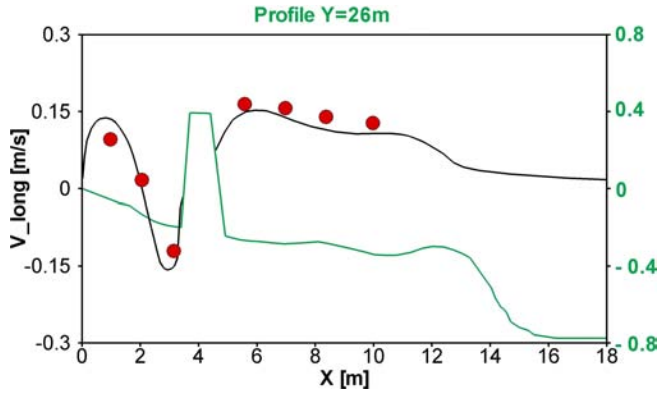

(a)

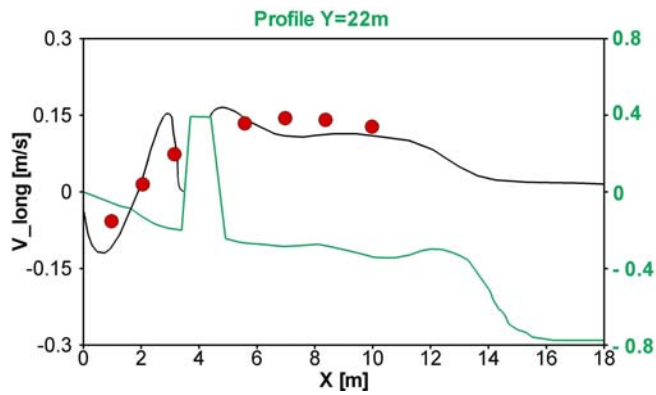

(b)

Fig. 10. Comparison of calculated (black lines) and measured (circles) longshore currents for Test T3C1 (beach profile in green line).

(gray line) are shown. From the comparison between Figs. 6 and 12 it is possible to deduce the bed changes produced by the numerical model. Such comparison reveal a salient development in the lee of the T-head groin and right near the stem: the 0.0–0.1 m depth contour lines advance toward the head section of about 1 m. The accretion in the updrift side of the stem is produced by the sediment put into suspension in the region upstream of the T-head groin (with respect to longshore current direction) and, in a smaller amount, by the sediment coming from the swash zone: the above sediment tends to accumulate in the lee of the T-head groin, due to the decay in the current velocity denoted by the presence of the above-mentioned first eddy. The accretion in the downdrift side of the stem is produced by the sediment coming from the swash zone and transported by the second eddy toward the stem.

From the comparison between Figs. 6 and 12, it is also possible to see the presence of two erosion areas in proximity of the head section extremes: a first erosion area

Coast. Eng. J. 2016.58. Downloaded from www.worldscientific.com
by UNIVERSITA DEGLI STUDI DI ROMA on 10/19/16. For personal use only.

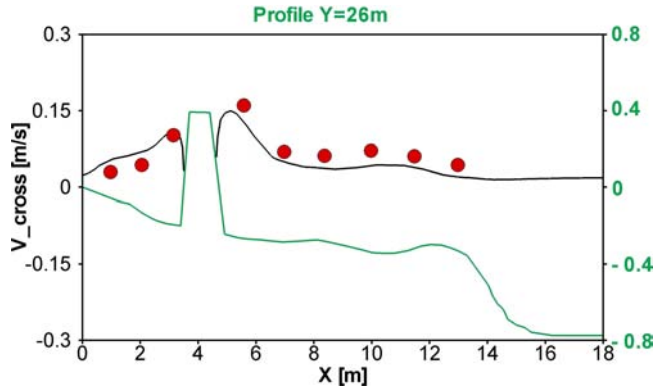

(a)

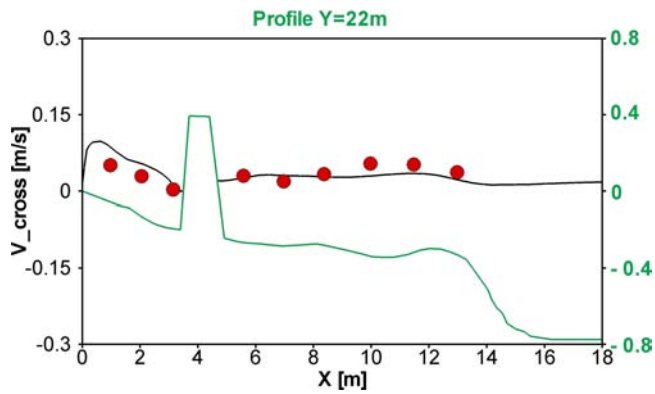

(b)

Fig. 11. Comparison of calculated (black lines) and measured (red circles) cross-shore currents for Test T3C1 (beach profile in green line).

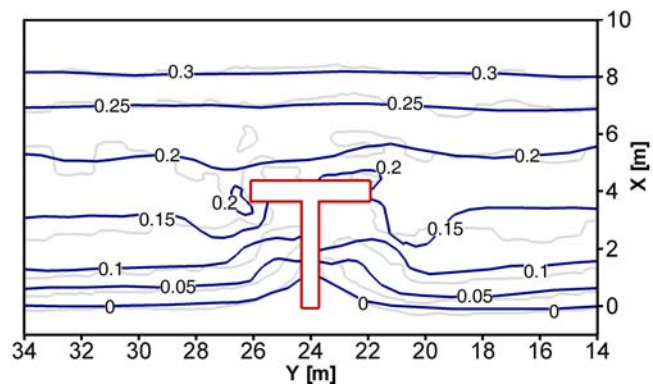

Fig. 12. Comparison of calculated (blue lines) and measured (gray lines) depth contour lines for Test T3C1.

Coast. Eng. J. 2016.58. Downloaded from www.worldscientific.com
by UNIVERSITA DEGLI STUDI DI ROMA on 10/19/16. For personal use only.

located close to the top left corner of the T-head groin ($3.5\,\text{m} < X < 4.5\,\text{m}$ and $26\,\text{m} < Y < 28\,\text{m}$) and highlighted by the presence of the 0.2 m depth contour line; a second erosion area near the bottom right corner of the T-head groin ($2.5\,\text{m} < X < 3.5\,\text{m}$ and $22\,\text{m} < Y < 20.5\,\text{m}$) and characterized by the retreat toward the shoreline of the 0.15-m depth contour line. Figure 12 also shows that the depth contour lines obtained at the end of the numerical simulation of Test T3C1 are in good agreement with the experimental data. The numerical results show a slight underestimation of the extension of the erosion area in the region near the shoreline located upstream of the T-head groin, between $Y = 32\,\text{m}$ and $Y = 28\,\text{m}$, and show a small underestimation of the extension of the erosion area in the region near to the shoreline downstream of the T-head groin ($Y > 21\,\text{m}$). From Fig. 12, it can further be seen that the numerical results slightly underestimate the extension of the erosion area near to the top left corner of the T-head groin and the salient updrift and downdrift of the T-head groin stem is overall reasonably well predicted.

Near the coastal defense structures, the current velocity field have a complex hydrodynamic configuration. Sediment put into suspension from the bottom by the breaking waves and sediment coming from the swash zone in the region upstream of the T-head groin are transported by longshore currents in the near area updrift the T-head groin stem and close to the shoreline: in this area, the sediment is carried away by the offshore-directed current and tends to settling in the lee of the T-head groin. The agreement between the numerical results and the experimental data shows that, in order to be able to simulate the bed morphological change phenomena produced by coastal structures normally connected to the shoreline, it is necessary to take into account the complexity of the phenomena, as already underlined at the end of the previous paragraph, such as: the undertow, the time variability of the intra-wave hydrodynamic quantities, the run-up and run-down in the swash zone and the related contribution to sediment transport.

The numerical models in which the advective sediment transport terms are calculated with the 2DHC approach (i.e. as a function of the product of the depth and wave-averaged horizontal velocity and the depth and wave-averaged suspended sediment concentration) are not able to take into account the cross-shore suspended sediment transport. Consequently, the agreement between the numerical results and the experimental data emphasizes the need to use the Q3D approach, in order to take into account the advective transport variations which occur at different depths and therefore to calculate the offshore–directed contribution of the cross-shore suspended sediment transport due to the undertow.

3.3. *Long-term bed evolution dynamics in morphologically articulated coastal region: the Pescara harbor*

The capacity of the proposed model to simulate sediment transport processes in morphologically articulated coastal regions, where slightly sloping and regular sea

Coast. Eng. J. 2016.58. Downloaded from www.worldscientific.com
by UNIVERSITA DEGLI STUDI DI ROMA on 10/19/16. For personal use only.

beds alternate with steep irregular bottoms and the coastlines can be characterized by complex shapes or be interrupted by the presence of anthropogenic structures and/or river mouths, is tested by numerically reproducing bed evolution dynamics in the coastal region opposite Pescara harbor in Italy.

In this subsection, the numerical results relating to two different morphological configurations of the coastal region opposite Pescara harbor are presented. The first set of results is produced by the numerical simulation of bed evolution dynamics occurred between 1997 and 2000 in the coastal region opposite Pescara harbor, in order to validate the model by comparing the simulated depth contour lines with that measured. The second set of results is produced by the numerical simulation of bed evolution dynamics in the present morphological configuration of the aforementioned coastal region.

In Fig. 13, the coastal structures in the near region of Pescara harbor are shown: the detached breakwater, entrance of the canal port, touristic port and eastern jetty are sketched by red lines, the designed submerged breakwater is sketched by dotted red lines, and the shoreline is sketched by a black line.

In the coastal region opposite Pescara harbor, at the end of 1997 a detached breakwater was built in order to protect the entrance of the canal port against

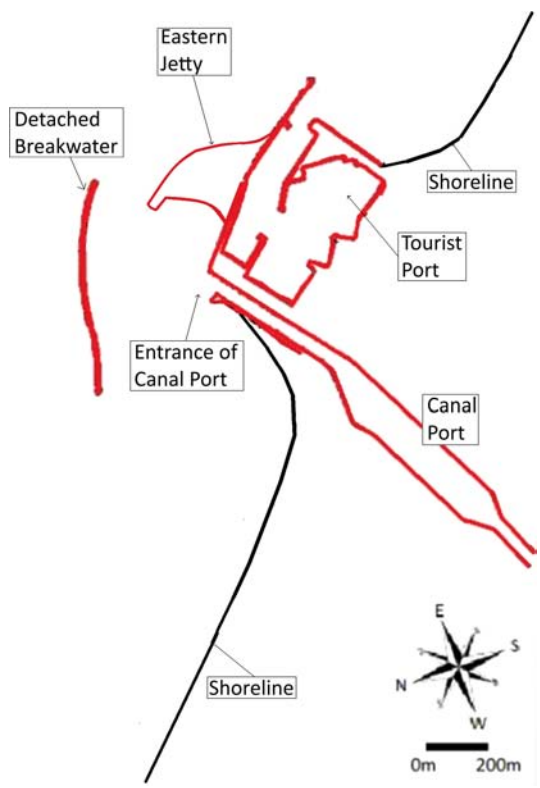

Fig. 13. Coastal structures in the near region of Pescara harbor.

Coast. Eng. J. 2016.58. Downloaded from www.worldscientific.com
by UNIVERSITA DEGLI STUDI DI ROMA on 10/19/16. For personal use only.

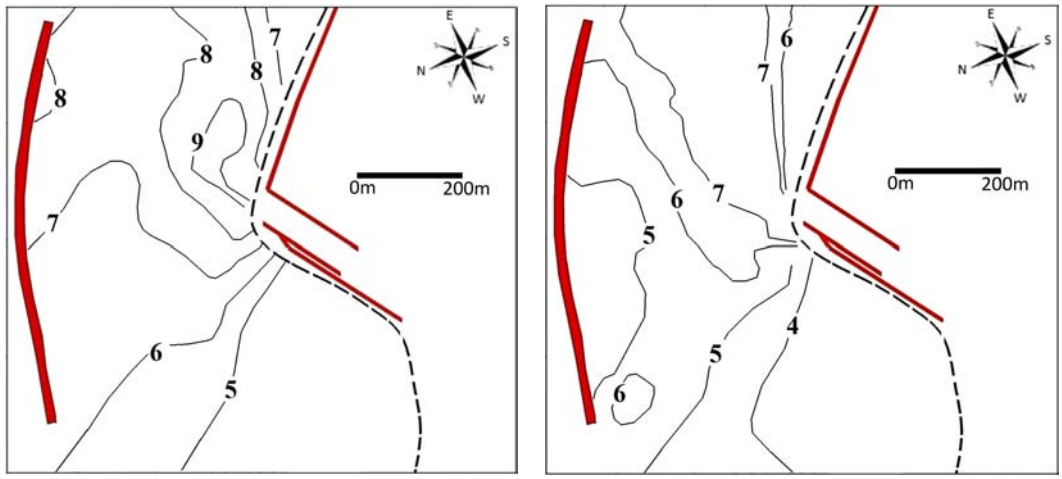

(a) (b)

Fig. 14. Measured depth contour lines in the coastal region opposite Pescara harbor in 1997 (a) and 2000 (b).

Coast. Eng. J. 2016.58. Downloaded from www.worldscientific.com
by UNIVERSITA DEGLI STUDI DI ROMA on 10/19/16. For personal use only.

dominant storms. After the detached breakwater construction, silting episodes occurred in the sea region included between the detached breakwater and entrance of the canal port.

Figures 14(a) and 14(b) illustrate respectively the above coastal region in 1997 and 2000: coastal structures are sketched by red lines, depth contour lines are sketched by black lines and the shoreline is sketched by a dashed black line. In 1997, the coastline showed up very articulated insofar as it was characterized by the presence of sandy beach stretches and vertical wall structures.

In that coastal region, two following bathymetric measurement campaigns were realized under the MEPLS [2008b]: the first one in 1997, right before the construction of the detached breakwater, and the second one in 2000, three years after the construction of the same structure; the resulting measured depth contour lines are respectively shown in Figs. 14(a) and 14(b). From the comparison between Figs. 14(a) and 14(b), the estimated annual sediment volume which accumulated in the sea region in question was about 40,000 m^3/year, according to MEPLS [2008b]. From the analysis of the two above-mentioned figures, it turns out that the above sea region was affected by silting phenomena; from the comparison between Figs. 14(a) and 14(b) two accretion areas are evident: the first one in correspondence of the entrance of canal port and the second one right rear of the detached breakwater.

In Fig. 15, the annual directional distribution of wave events inshore Pescara coastal region is given (such as reported in MEPLS [2008a]). From Fig. 15, it can be seen that the distribution of wave events has a dual mode structure with the main directions of wave rays originating from the primary sector 345°N–15°N and from the secondary sector 65°N–95°N.

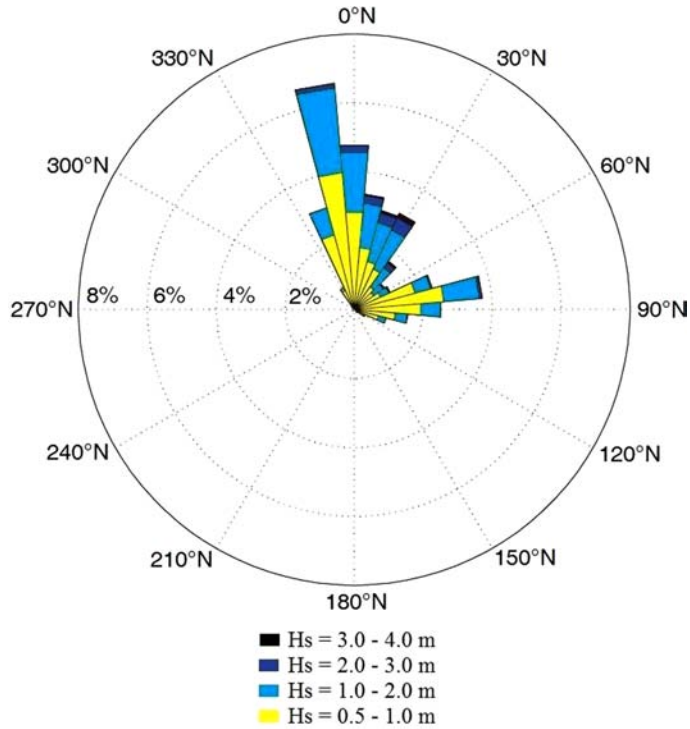

Fig. 15. Directional annual distribution polar histogram of the wave events in the coastal region opposite Pescara harbor.

Wave trains originating from the primary sector produce a South–East directed longshore current. In the stretch of coast north of the canal port, the sediment material is put into suspension by the wave breaking and transported by the above-mentioned longshore current in South–East direction. Such suspended sediment material tends to deposit in the sea region included between the detached breakwater and entrance of the canal port because the wave energy is significantly beaten down by the shielding effect of the detached breakwater.

Wave trains originating from the secondary sector produce a North–West directed longshore current. The MEPLS [2008b] states that the North–West directed sediment transport does not significantly contribute to silting up in that sea region. As reported in that study, indeed it can be assumed that the sediment transport related to the secondary sector is intercepted almost completely by the tourist port (sketched by red lines in Fig. 13), before reaching the aforementioned sea region.

Consequently the silting up in the sea region included between the detached breakwater and entrance of the canal port is produced by waves originating from the primary sector (345°N–15°N) that entail a South–East directed longshore sediment transport. It follows from the above that the simulation of bed morphological changes can be carried out starting from the wave features related to the primary sector as deduced from Fig. 15. As can be seen from Fig. 15, the most frequent wave events

Coast. Eng. J. 2016.58. Downloaded from www.worldscientific.com
by UNIVERSITA DEGLI STUDI DI ROMA on 10/19/16. For personal use only.

originating from the primary sector are characterized by a significant wave height of 1.5 m and act not less than 320 h/year.

Therefore, the above-mentioned wave height, direction and occurrence frequency, and the depth contour lines shown in Fig. 14(a) are used as input data in the numerical simulations of the bed evolution dynamics occurred from 1997 to 2000; in particular the random wave trains are numerically generated by using a JONSWAP frequency spectrum.

The equations of the hydrodynamic model (described in Sec. 2.1) are integrated on a curvilinear boundary conforming computational grid whose boundaries are represented in Fig. 16 by a dashed black line. Such boundaries are obtained by means of a Shoaling–Refraction model applied over a computational domain which represents a more extended sea region than that included by the above-mentioned curvilinear grid. In particular, the North–West and South–East (lateral) boundaries

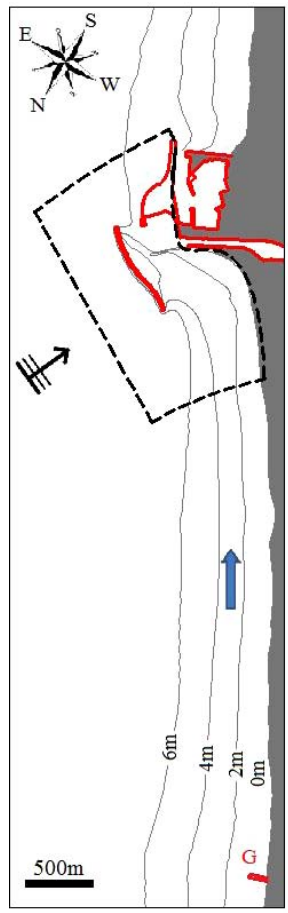

Fig. 16. Pescara coastal area: coastal defense structures (solid red lines); bathymetric lines (solid gray lines); longshore current (blue arrow) produced by the most frequent wave event (black arrow); computational domain for the hydrodynamic and morphodynamic model (dashed black line).

Coast. Eng. J. 2016.58. Downloaded from www.worldscientific.com
by UNIVERSITA DEGLI STUDI DI ROMA on 10/19/16. For personal use only.

of the curvilinear grid coincide with the wave rays, as calculated by the Shoaling–Refraction model. Hence, the null value of the normal derivative of the instantaneous velocity and free surface elevation is set at the above-mentioned boundaries. The North–East (upper) boundary coincides with the line identified by the wave front at deep water, as calculated by the Shoaling–Refraction model. Along this boundary an internal wave generation zone is located, offshore from which a grid extension and a dissipation zone (sponge zone) are introduced in order to avoid the reflections incoming from deep water. Along the stretch of coast characterized by a sandy beach, a wet and dry technique is used; along the stretch of coast interested by structure reflective boundary conditions are imposed.

The equations of the morphodynamic model (described in Sec. 2.2) are integrated on the same curvilinear grid adopted for the hydrodynamic model (whose boundaries are represented in Fig. 16 by a dashed black line). In Fig. 16, it is observed that the stretch of coast located North–West with respect to Pescara harbor is characterized by a straight shoreline and shows a cylindrical bathymetry. In the above-mentioned stretches of coast under the wave event originating from the primary sector (345°N–15°N), a longshore current (whose direction is indicated by the blue arrow in Fig. 16) occurs. Consequently, downstream the groin structure located in G (Fig. 16) and at sufficient distance from this, the depth and wave-averaged longshore current velocities are almost constant along the trajectories. Such constant conditions along the trajectories permain as far as the shoreline is straight and the bathymetry is cylindrical. In the same stretch of coast also the wave-averaged bed load transport and wave-averaged suspended sediment concentration values are almost constant along the trajectories. Since the North–West boundary of the curvilinear grid is included in the sea region where these constant conditions along the trajectories occur, at this boundary the null normal derivative of the wave-averaged suspended sediment concentration and wave-averaged bed load transport is assigned. Analogous boundary conditions of the null normal derivative are assigned even at the South–East and North–East lateral boundaries. Concerning the other boundaries, in the stretch of coast characterized by a sandy beach the boundary of the computational domain for the numerical integration of the advection–diffusion equation for the suspended sediment concentration is placed at the border between the inner surf zone and the swash zone at the location of the start of the uprush. At this boundary, the sediment transport obtained from the swash zone computation is used as the boundary value for the numerical solution of the above-mentioned equation (as described in Sec. 2.2). In the stretch of coast affected by structures a null sediment flux at the boundary is imposed.

The time discretization step for the 2DPR hydrodynamic model and for the advection–diffusion equation for the suspended sediment concentration is 0.1 s.

The simulation of the bed morphological change which took place from 1997 to 2000 is performed by using a sequence of 240 morphological steps. Each morphological step corresponds to a bed morphological change over a time interval equal to 4 h

Coast. Eng. J. 2016.58. Downloaded from www.worldscientific.com
by UNIVERSITA DEGLI STUDI DI ROMA on 10/19/16. For personal use only.

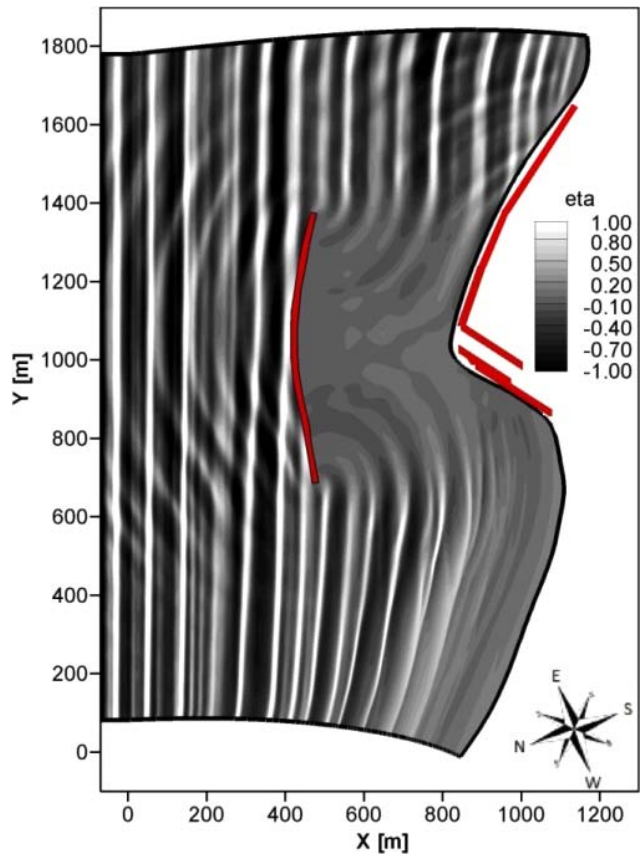

Fig. 17. Instantaneous wave field in the coastal region opposite Pescara harbor in 1997.

(morphological time step) and requires the consecutive application of the numerical models described in Sec. 2. It has been observed that, for the Pescara harbor case, greater values than 8 h for the morphological time step (even if more efficient from a computational point of view) produce an unrealistic evolutive dynamics.

In Fig. 17, an instantaneous wave field, obtained starting from the initial bathymetry shown in Fig. 14(a) and wave features deduced by Fig. 15, is shown. It can be seen from the figure that wave trains not intercepted by the detached breakwater show first a steepening front of the wave height (shoaling) and then a decay of the wave height due to the breaking. In the vicinity of the West and East, extremes of the detached breakwater wave fronts undergo a rotation by diffraction.

In Fig. 18 the wave-averaged velocity field is shown: the presence of a longshore current which is directed from North–West to South–East can be seen. The values of the simulated current velocity are compared with that measured in the three points indicated in the same figure (the measured current velocity are taken at middle of water depth and during a wave event originating from 0°N and characterized by a wave height of 1.5 m). In Table 2, the values of simulated and measured current

Coast. Eng. J. 2016.58. Downloaded from www.worldscientific.com
by UNIVERSITA DEGLI STUDI DI ROMA on 10/19/16. For personal use only.

Coast. Eng. J. 2016.58. Downloaded from www.worldscientific.com
by UNIVERSITA DEGLI STUDI DI ROMA on 10/19/16. For personal use only.

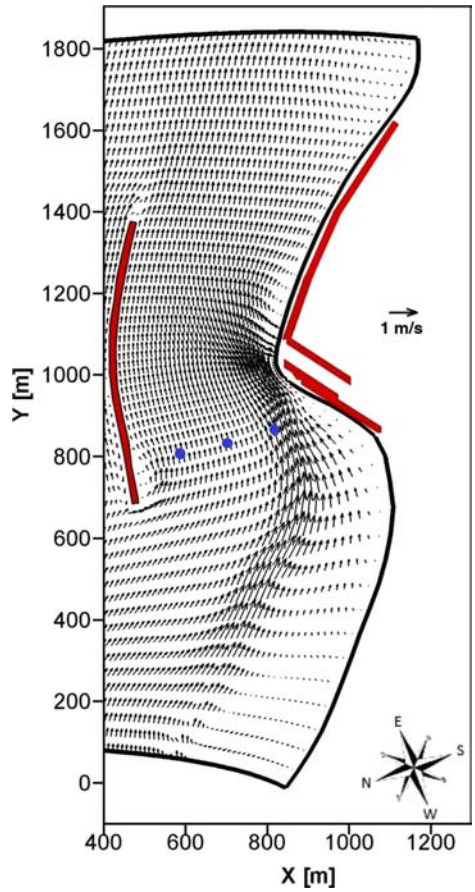

Fig. 18. Calculated wave-averaged velocity field (black vectors) and location of measurement points (blue points) in the coastal region opposite Pescara harbor in 1997.

Table 2. Comparison between calculated and measured current velocities in the three measurements points in the coastal region opposite Pescara harbor.

Point of measure	Coordinates		Experimental Data			Numerical Results		
	X(m)	Y(m)	Vx (m/s)	Vy (m/s)	V (m/s)	Vx (m/s)	Vy (m/s)	V (m/s)
VI	585	805	−0.035	0.326	0.328	−0.045	0.265	0.269
V2	705	835	−0.043	0.179	0.184	−0.053	0.236	0.242
V3	820	880	−0.217	0.649	0.684	−0.175	0.503	0.533

velocity, under wave conditions whose features are the same as the wave events used as input for the numerical simulations, are given: from this comparison a good agreement can be seen between the numerical results and field data.

Figure 19 illustrates the depth contour lines at the end of the third simulated year obtained by using the proposed weakly-coupled model and starting from the initial bathymetry (shown in Fig. 14(a)). Depth contour lines at the end of the third

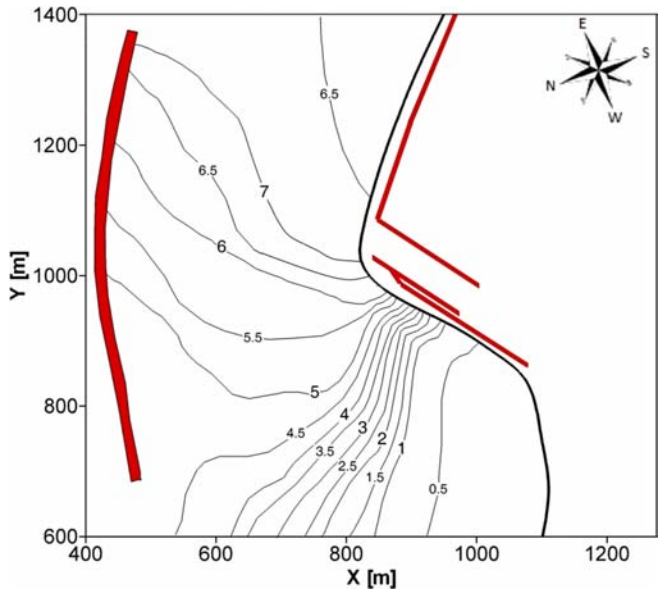

Fig. 19. Calculated depth contour lines at the end of third year for numerical simulation in the coastal region opposite Pescara harbor in 2000.

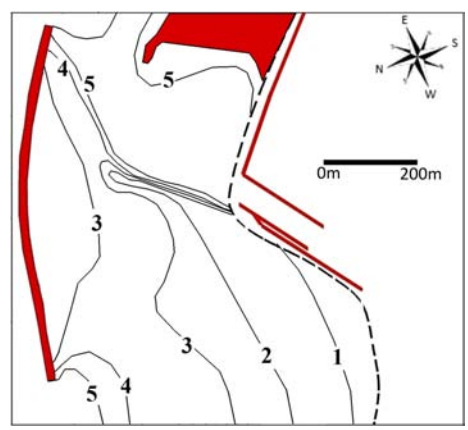

Fig. 20. Measured depth contour lines in the coastal region opposite Pescara harbor in 2014.

simulated year (Fig. 19) are in agreement with those obtained from the measurement campaign conducted in 2000 (Fig. 14(b)). In particular, from the comparison between the simulated depth contour lines and the initial bathymetry, two accretion areas are evident: one right in front of the entrance of the canal port and the other right near the downdrift side of the detached breakwater, consistent with what observed from the comparison between depth contour lines obtained from the bathymetric measurement campaigns in 1997 and 2000. Furthermore, as mentioned, the above comparison gives an accumulated sediment volume in the sea region in

Coast. Eng. J. 2016.58. Downloaded from www.worldscientific.com
by UNIVERSITA DEGLI STUDI DI ROMA on 10/19/16. For personal use only.

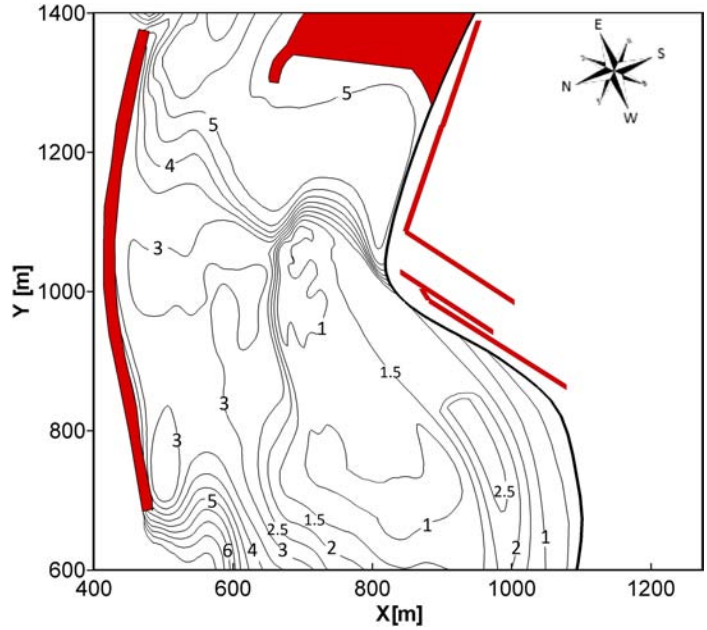

Fig. 21. Calculated depth contour lines at the end of third year for numerical simulation in the coastal region opposite Pescara harbor.

question of about 40,000 m^3/year. The numerical simulation of the bed changes calculates a settled sediment volume, in the same region, of about 38,500 m^3/year.

The numerical simulation satisfactorily reproduces the bed morphological changes in the coastal region opposite Pescara harbor. The numerical results demonstrated that the proposed model is able to represent generally well the long-term bed evolution dynamics and to identify qualitatively well the main accretion and erosion areas in coastal region morphologically articulated even in presence of coastal defense structures, as in the case of the coastal region opposite Pescara harbor.

The model thus tuned is used for the prediction of bed evolution dynamics in the present morphological configuration of the aforementioned coastal region.

In Fig. 20, the present configuration of the coastal region opposite Pescara harbor (2015) and the related depth contour lines in the outer harbor region are shown (such as reported in MIT [2008b]). From this figure, it can be observed that, with respect to what happened in 2000, the bed levels have overall increased in the sea region included between the detached breakwater and entrance of the canal port and thus silting phenomena still occur in this area. In the vicinity of the entrance of the canal port, the sharp decrease in the bed levels is due to the dredging operations for the maintenance of navigability conditions. Furthermore the presence of an eastern jetty (built in 2005) can be seen.

Hereafter the numerical results obtained by means of the proposed model starting from the initial bathymetry are presented as shown in Fig. 20.

Coast. Eng. J. 2016.58. Downloaded from www.worldscientific.com
by UNIVERSITA DEGLI STUDI DI ROMA on 10/19/16. For personal use only.

In Fig. 21, the depth contour lines at the end of the third simulated year are shown. From the comparison between Figs. 21 and 20, it can be observed a general bed level increment in the sea region included between the detached breakwater and entrance of the canal port; in particular two main accretion areas are observed, similar to that realized during the three year period 1997–2000. The first of the above-mentioned areas is located in correspondence of the entrance of the canal port (related to the advancement from South–West to North–East of 1–3 m depth contour lines) and the second area is located close to the downdrift side of the West extreme of the detached breakwater (highlighted by the emergence of the 3-m depth contour line).

The numerical simulation calculates a settled sediment volume in the sea region in question of about 37,000 m^3/year: This value is of the same order of magnitude as the annual accumulated sediment volume in the three year period 1997–2000 (as estimated from the above-mentioned 1997 and 2000 bathymetric measurement campaigns).

Coast. Eng. J. 2016.58. Downloaded from www.worldscientific.com
by UNIVERSITA DEGLI STUDI DI ROMA on 10/19/16. For personal use only.

4. Conclusions

In this paper, we have proposed a model for the simulation of the bed evolution dynamics in coastal regions characterized by articulated morphologies.

An integral form of the FNBEs in contravariant formulation, in which Christoffel symbols are absent, has been proposed in order to simulate the hydrodynamic fields.

The bed evolution dynamics have been calculated starting from the contravariant formulation of the advection–diffusion equation for the suspended sediment concentration and taking into account the contribution given by the spatial variation of the bed load transport.

It has been emphasized that in order to be able to predict the bed morphological evolution in coastal regions characterized by articulated morphologies, it is essential: (a) to take into account the undertow; (b) to take into account the variability in the wave period of the intra-wave hydrodynamic quantities; (c) to use a quasi-three-dimensional approach for the advective sediment transport terms in the advection–diffusion equation for the suspended sediment concentration.

The ability of the proposed model to simulate sediment transport phenomena in a coastal region morphologically articulated has been verified comparing numerical results, obtained by the simulation of long-term bed evolution dynamics in the coastal region opposite Pescara harbor in Italy, with the field data.

Appendix A

$$\vec{s} = H\left\{\left[\frac{\sigma^2}{2} - \frac{1}{6}(h^2 - h\eta + \eta^2)\right]\nabla\left(\nabla\cdot\frac{\vec{r}}{H}\right) + \left[\sigma + \frac{1}{2}(h-\eta)\right]\nabla\left[\nabla\cdot\left(h\frac{\vec{r}}{H}\right)\right]\right\}, \tag{A.1}$$

$$\vec{V}' = \frac{1}{2}\sigma^2\nabla\left(\nabla\cdot\frac{\vec{r}}{H}\right) + \sigma\nabla\left(\nabla\cdot h\frac{\vec{r}}{H}\right) - \nabla\left[\frac{1}{2}\eta^2\left(\nabla\cdot\frac{\vec{r}}{H}\right) + \eta\left(\nabla\cdot h\frac{\vec{r}}{H}\right)\right], \quad \text{(A.2)}$$

$$\vec{V}'' = \nabla\left[\frac{\partial}{\partial t}\left(\frac{\eta^2}{2}\right)\nabla\cdot\frac{\vec{r}}{H}\right] + \nabla\left[\frac{\partial\eta}{\partial t}\nabla\cdot\left(h\frac{\vec{r}}{H}\right)\right], \quad \text{(A.3)}$$

$$\vec{T} = \nabla\left\{(\sigma-\eta)\left(\frac{\vec{r}}{H}\cdot\nabla\right)\left[\nabla\cdot\left(h\frac{\vec{r}}{H}\right)\right] + \frac{1}{2}(\sigma^2-\eta^2)\left(\frac{\vec{r}}{H}\cdot\nabla\right)\left(\nabla\cdot\frac{\vec{r}}{H}\right)\right\}$$
$$+ \frac{1}{2}\nabla\left\{\left[\nabla\cdot\left(h\frac{\vec{r}}{H}\right) + \eta\nabla\cdot\frac{\vec{r}}{H}\right]^2\right\}, \quad \text{(A.4)}$$

$$\vec{W} = \hat{i}\left[\Omega\left(-\frac{s_y}{H}\right) - \Theta\left(-\frac{r_y}{H}\right)\right] + \hat{j}\left[\Omega\left(\frac{s_x}{H}\right) - \Theta\left(\frac{r_x}{H}\right)\right], \quad \text{(A.5)}$$

in which

$$\Omega = \left[\frac{\partial}{\partial x}\left(\frac{r_y}{H}\right) - \frac{\partial}{\partial y}\left(\frac{r_x}{H}\right)\right] \quad \text{and} \quad \Theta = \left[\frac{\partial}{\partial x}\left(\frac{s_x}{H}\right) - \frac{\partial}{\partial y}\left(\frac{s_y}{H}\right)\right],$$

$$s^l = (h+\eta)\left\{\left[\frac{\sigma^2}{2} - \frac{1}{6}(h^2 - h\eta + \eta^2)\right]g^{lm}\left[\left(\frac{r^k}{H}\right)_{,k}\right]_{,m}\right.$$
$$\left. + \left[\sigma + \frac{1}{2}(h-\eta)\right]g^{lm}\left[\left(h\frac{r^k}{H}\right)_{,k}\right]_{,m}\right\}, \quad \text{(A.6)}$$

$$V'^l = \frac{1}{2}\sigma^2 g^{lm}\left[\left(\frac{r^k}{H}\right)_{,k}\right]_{,m} + \sigma g^{lm}\left[\left(h\frac{r^k}{H}\right)_{,k}\right]_{,m}$$
$$- g^{lm}\left[\frac{1}{2}\eta^2\left(\frac{r^k}{H}\right)_{,k} + \eta\left(h\frac{r^k}{H}\right)_{,k}\right]_{,m}, \quad \text{(A.7)}$$

$$V''^l = g^{lm}\left[\frac{\partial}{\partial t}\left(\frac{\eta^2}{2}\right)\left(\frac{r^k}{H}\right)_{,k}\right]_{,m} + g^{lm}\left[\frac{\partial\eta}{\partial t}\left(h\frac{r^k}{H}\right)_{,k}\right]_{,m}, \quad \text{(A.8)}$$

$$T^l = g^{lm}\left\{(\sigma-\eta)\left(\frac{r^i}{H}\left[\left(h\frac{r^k}{H}\right)_{,k}\right]_{,i}\right) + \frac{1}{2}(z_\alpha^2 - \eta^2)\left(\frac{r^i}{H}\left[\left(\frac{r^k}{H}\right)_{,k}\right]_{,i}\right)\right\}_{,m}$$
$$+ \frac{1}{2}g^{lm}\left\{\left[\left(h\frac{r^k}{H}\right)_{,k} + \eta\left(\frac{r^k}{H}\right)_{,k}\right]^2\right\}_{,m}, \quad \text{(A.9)}$$

Coast. Eng. J. 2016.58. Downloaded from www.worldscientific.com
by UNIVERSITA DEGLI STUDI DI ROMA on 10/19/16. For personal use only.

$$W^l = \left(\varepsilon^{mi} g_{ip} \frac{r^p_{,m}}{H}\right) \varepsilon^{jl} \frac{s_j}{H} + \left(\varepsilon^{mi} g_{ip} \frac{s^p_{,m}}{H}\right) \varepsilon^{jl} \frac{r_j}{H} \tag{A.10}$$

in which

$$\varepsilon^{mi} = \begin{cases} \dfrac{1}{\sqrt{g}} & \text{if } (m,i) \text{ is an even permutation of } (1,2) \\ -\dfrac{1}{\sqrt{g}} & \text{if } (m,i) \text{ is an odd permutation of } (1,2) \\ 0 & \text{if the two indices are equal.} \end{cases}$$

Coast. Eng. J. 2016.58. Downloaded from www.worldscientific.com
by UNIVERSITA DEGLI STUDI DI ROMA on 10/19/16. For personal use only.

Appendix B

The system composed of Eqs. (20), (23) and (24) is numerically solved following the procedure shown below, which permits the calculation of $\tilde{C}_a$ and $\tilde{C}(z)$.

The time integration of Eq. (20) is carried out by means of a third order accurate SSPRK method reported in Spiteri and Ruuth [2002]. Such integration permits the calculation of the depth and wave-averaged suspended sediment concentration $\bar{\tilde{C}}$, at time t_0, i.e. $\bar{\tilde{C}}|_{t_0}$.

Equation (23) analytically integrated over z between the level a from the bottom, where the actual concentration $\tilde{C}_a$ is calculated, and a generic level z, where the wave-averaged suspended sediment concentration $\tilde{C}(z)$ is defined, gives the following expression for $\tilde{C}(z)$

$$\tilde{C}(z) = \tilde{C}_a \cdot e^{-\int_a^z (w_{\text{sed}}/\tilde{\nu}_t(z))dz}. \tag{B.1}$$

Once $\bar{\tilde{C}}|_{t_0}$ is known, starting from an initial value of the actual concentration $\tilde{C}^1_a|_{t_0}$ an iterative calculation procedure is activated which, at the generic step n, can be shown as

$$\tilde{C}(z)^n|_{t_0} = \tilde{C}^n_a|_{t_0} \cdot e^{-\int_a^z (w_{\text{sed}}/\tilde{\nu}_t(z)\tilde{\nu}_t(z))dz} \tag{B.2}$$

$$\bar{\tilde{C}}^n|_{t_0} = \frac{1}{\tilde{H}} \int_a^{\tilde{H}} \tilde{C}(z)^n|_{t_0} dz \tag{B.3}$$

$$\bar{\tilde{C}}^n|_{t_0} - \bar{\tilde{C}}|_{t_0}| = \Delta\bar{\tilde{C}}|_{t_0} \tag{B.4}$$

$$\begin{cases} \text{se } \Delta\bar{\tilde{C}}|_{t_0} > \text{eps} \;\rightarrow \tilde{C}^{n+1}_a|_{t_0} = \tilde{C}^n_a|_{t_0} + \Delta C_a \rightarrow \text{Eq. (B.1)} \\ \text{se } \Delta\bar{\tilde{C}}|_{t_0} \le \text{eps} \;\rightarrow \tilde{C}_a|_{t_0} = \tilde{C}^n_a|_{t_0}; \quad \tilde{C}(z)|_{t_0} = \tilde{C}(z)^n|_{t_0} \end{cases} \tag{B.5}$$

The new value of the depth and wave-averaged suspended sediment concentration $\bar{\tilde{C}}$ at the new time $t_0 + \Delta t_c$, i.e. $\bar{\tilde{C}}|_{t_0+\Delta t_c}$ is obtained by solving Eq. (20) where the sediment deposition rate term D, given by Eq. (21), is set equal to $w_{\text{sed}}\tilde{C}_a|_{t_0}$.

The above-mentioned numerical procedure, used to solve the set of Eqs. (20), (23) and (24) is repeated until Eq. (20) reaches a stationary state.

References

Camenen, B. & Larson, M. [2008] "A general formula for non cohesive suspended sediment transport," *J. Coastal Res.* **24**(3), 615–627.

Choi, J. & Yoon, S. B. [2008] "A three-dimensional numerical simulation of wave and current evolving over a submerged shoal," *Coastal Eng. J.* **53**(02), 63–85.

Cioffi, F. & Gallerano, F. [2012] "Multi-objective analysis of dam release flows in rivers downstream from hydropower reservoirs," *Appl. Math. Modell.* **36**(7), 2868–2889.

Deigaard, R., Fredsoe, J. & Hedegaard, I. B. [1986] "Suspended sediment in the surf zone," *J. Waterway, Port, Coastal Ocean Engin.* **112**(1), 115–128.

Deigaard, R., Justensen, P. & Fredsoe, J. [1991] "Modelling of undertow by a one equation turbulence model," *Coastal Eng.* **5**(5–6), 431–458.

Dronen, N. & Deigaard, R. [2007] "Quasi-three-dimensional modelling of the morphology of longshore bars," *Coastal Eng.* **54**(3), 197–215.

Engelund, F. & Fredsøe, J. [1976] "A sediment transport model for straight alluvial channels," *Nordic Hydrol.* **7**, 293–306.

Fredsøe, J. [1984] "Turbulent boundary layer in wave-current motion," *J. Hydraulic Eng.* **110**, 1103–1120.

Fredsøe, J., Andersen, O. H. & Silberg, S. [1985] "Distribution of suspended sediment in large waves," *J. Waterway, Port, Coastal Ocean Eng.* **111**(6), 1041–1059.

Gallerano, F. & Cannata, G. [2011a] "Central WENO scheme for the integral form of contravariant shallow-water equations," *Int. J. Numeri. Meth. Fluids* **67**(8), 939–959.

Gallerano, F. & Cannata, G. [2011b] "Compatibility between reservoir sediment flushing and river protection," *J. Hydraulic Eng.* **137**(10), 1111–1125.

Gallerano, F., Cannata, G. & Tamburrino, M. [2012] "Upwind WENO scheme for shallow water equations in contravariant formulation," *Computers & Fluids* **62**, 1–12.

Gallerano, F., Cannata, G. & Villani, M. [2014] "An integral contravariant formulation of the fully non-linear Boussinesq equations," *Coastal Eng.* **83**, 119–136.

Gravens, M. B. & Wang, P. [2007] "Data Report: LSTF Experiments — Transport by Waves and Currents & Tombolo Development Behind Headland Structures, Technical Report ERDC/CHLTR-04-9," *Coastal and Hydraulics Laboratory, US Army Engineer Research and Development Center Vicksburg MS.*

Hsiao, S. C. & Hsu, C. M. [2011] "Wave transformation over an elliptic shoal on a sloping bottom," *Coastal Eng. J.* **53**(2), 151–176.

Hsu, T. J., Helgar, S. & Guza, R. T. [2006] "Wave-induced sediment transport and onshore sandbar migration," *Coastal Eng.* **53**, 817–824.

Jayaratne, M. P. R. & Shibayama, T. [2007] "Suspended sediment concentration on beaches under three different mechanism" *Coastal Eng. J.* **49**(04), 357–392.

Jayaratne, M. P. R., Rahman, M. R. & Shibayama, T. [2014] "A cross-shore beach profile evolution model," *Coastal Eng. J.* **56**(4), 1–70.

Kalinske, A. A. [1947] "Movement of sediment as bed load in rivers," *Transactions, American Geophysical Union* **28**(4), 615–620.

Kennedy, A. B., Chen, Q., Kirby, J. T. & Darlrymple, R. A. [2000] "Boussinesq modeling of wave transformation, breaking, and runup. I:1D," *J. Waterway, Port, Coastal, Ocean Eng.* **126**(1), 39–47.

Larson, M., Kubota, S. & Erikson, L. [2004] "Swash-zone sediment transport and foreshore evolution: Field experiments and mathematical modeling," *Marine Geol.* **212**, 31–79.

Larson, M. & Wamsley, T. V. [2007] "A formula for longshore sediment transport in the swash," *Coastal Sediments* **7**, 1924–1937.

Coast. Eng. J. 2016.58. Downloaded from www.worldscientific.com
by UNIVERSITA DEGLI STUDI DI ROMA on 10/19/16. For personal use only.

Li, B., Yu, X. & Yu, Y. [2007] "Nonlinear dynamics of nearshore irregular waves: A three-dimensional numerical model and its validation," *Coastal Eng. J.* **49**(02), 103–126.

Longuet-Higins, M. S. & Stewart, R. [1964] "Radiation stresses in water waves; a physical discussion, with applications," *Deep-Sea Res.* **2**, 529–562.

Luo, H. & Bewley, T. R. [2004] "On the contravariant form of the Navier–Stokes equation in time-dependent curvilinear coordinate systems," *J. Comput. Phys.* **199**(1), 355–375.

Lynett, P. J. [2006] "Nearshore wave modeling with high-order Boussinesq-type equations," *J. Waterway, Port, Coastal Ocean Eng.* **132**, 348–357.

Ma, G., Chou, Y.-J. & Shi, F. [2014] "A wave-resolving model for nearshore suspended sediment transport," *Ocean Modell.* **77**, 33–49.

Mandal, J. & Rao, S. P. [2011] "High resolution finite volume computations on unstructured grids using solution dependent weighted least squares gradients," *Comput. Fluids* **44**(1), 23–31.

Mather, A., Stretch, D. & Garland, G. [2011] "Predicting extreme wave run-up on natural beaches for coastal planning and management," *Coastal Eng. J.* **53**(02), 87–109.

Ministry of the Environment and Protection of Land and Sea [2008a] "Studio Meteomarino — Piano Regolatore Portuale del Porto di Pescara," p. 14, available at: www.va.minambiente.it.

Ministry of the Environment and Protection of Land and Sea [2008b] "Studio Morfologico — Piano Regolatore Portuale del Porto di Pescara," p. 22–24, available at: www.va.minambiente.it.

Mohsin, S. & Tajima, Y. [2014] "Modeling of time-varying shear current field under breaking and broken waves with surface rollers," *Coastal Eng. J.* **56**(3).

Nam, P. T., Larson, M., Hanson, H. & Hoan, L. X. [2009] "A numerical model of nearshore waves, currents, and sediment transport," *Coastal Eng.* **56**(11–12), 1084–1096.

Nam, P. T., Larson, M., Hanson, H. & Hoan, L. X. [2011] "A numerical model of beach morphological evolution due to waves and currents in the vicinity of coastal structures," *Coastal Eng.* **58**, 863–876.

Nam, P. T., Oumeraci, H., Larson, M. & Hanson, H. [2014] "Modeling undertow due to random waves," *Ocean Dynam.* **64**, 1209–1219.

Nwogu, O. [1993] "An alternative form of the Boussinesq equations for nearshore wave propagation," *J. Waterway, Port, Coastal Ocean Eng.* **119**, 618–638.

Rakha, K. A., Deigaard, R. & Brøker, I. [1997] "A phase-resolving cross shore sediment transport model for beach profile evolution," *Coastal Eng.* **31**(1–4), 231–261.

Rakha, K. A. [1998] "A Quasi-3D phase-resolving hydrodynamic and sediment transport model," *Coastal Eng.* **34**, 277–311.

Rakha, K. A. [2002] "Numerical study of different boundary conditions for undertow models," *Coastal Eng. J.* **45**(02), 163–187.

Roelvink, J. A. & Reniers, A. J. H. M. [1995] "LIP 11D Delta Flume experiments, A data set for profile model validation, Report H2130," *Delft Hydraulics*, The Netherlands.

Shi, F. & Sun, W. [1995] "A variable boundary model of storm surge flooding in generalized curvilinear coordinate grids," *Int. J. Numer. Meth. Fluids* **21**, 641–651.

Shi, F., Kong, Y. & Ding, P. [1998] "An implicit method using contravariant velocity components and calculations in a harbor-channel area," *Acta Oceanologica Sinica* **20**(4), 17–24.

Shi, F., Kirby, J. T., Harris, J. C., Geiman, J. D. & Grilli, S. T. [2012] "A high-order adaptive time stepping TVD solver for Boussinesq modeling of breaking waves and coastal inundation," *Ocean Modell.* **43–44**, 36–51.

Shibayama, T. & Nistor, I. [1998] "Modelling of time-dependent sand transport at the bottom boundary layer in the surf zone," *Coastal Eng. J.* **40**, 241.

Spiteri, R. J. & Ruuth, S. J. [2002] "A new class of optimal high-order strong-stability preserving time discretization methods," *SIAM J. Numer. Anal.* **40**(2), 469–491.

Titarev, V. & Drikakis, D. [2011] "Uniformly high-order schemes on arbitrary unstructured meshes for advection–diffusion equations," *Comput. Fluids* **46**(1), 467–471.

Van Rijn, L. C. [1984a] "Sediment transport, Part I: Bed load transport," *J. Hydraulic Eng.* **110**(10), 1431–1456.

Coast. Eng. J. 2016.58. Downloaded from www.worldscientific.com
by UNIVERSITA DEGLI STUDI DI ROMA on 10/19/16. For personal use only.

Wai, O. W. H., Chen, Y. & Li, Y. S. [2004] "A3-d wave–current driven coastal sediment transport model," *Coastal Eng. J.* **46**(4), 385–424.

Wei, G., Kirby, J. T., Grill1, S. T. & Subramanya, R. [1995] "A fully non-linear Boussinesq model for surface waves. Part 1. Highly non-linear unsteady waves," *J. Fluid Mech.* **294**, 71–92.

Zyserman, J. A., Fredsoe, J. [1994] "Data analysis of bed concentration of suspended sediment," *J. Hydraulic Eng.* **120**(9), 1021–1042.

Coast. Eng. J. 2016.58. Downloaded from www.worldscientific.com
by UNIVERSITA DEGLI STUDI DI ROMA on 10/19/16. For personal use only.